Clim Dyn (2013) 41:1569–1594
DOI 10.1007/s00382-012-1631-6

Boreal summer intraseasonal variability simulated in the NCEP climate forecast system: insights from moist static energy budget and sensitivity to convective moistening

K. P. Sooraj · Kyong-Hwan Seo

Received: 16 June 2012 / Accepted: 10 December 2012 / Published online: 25 December 2012

Abstract The NCEP Climate Forecast System (CFS) with the relaxed Arakawa Schubert (RAS, hereafter referred to as CTRL) convection scheme of Moorthi and Suarez exhibits better performance in representing boreal summer tropical intraseasonal variability as compared with a simulation using simplified Arakawa–Schubert scheme. The intraseasonal moist static energy (MSE) budget is analyzed in this version of the CFS model (CTRL), which produces realistic eastward and northward propagation characteristics. The moist and thermodynamic processes involved in the maintenance and propagation of the poleward moving intraseasonal oscillation (ISO) disturbances are examined here. Budget diagnostics show that horizontal MSE advection is the principal component of the budget, contributing to the poleward movement of the convection. The injection of MSE moistens the atmosphere north of the convective area causing the poleward movement of convection by destabilization of the atmosphere. The moistening process is mainly contributed by the climatological wind acting on the anomalous moisture gradient as confirmed from the examination of moisture advection equation. While surface enthalpy fluxes (consisting of radiative and surface turbulent heat fluxes) maintain the ISO anomalies, they oppose the MSE tendency due to horizontal advection thus regulating the poleward propagation characteristics. In addition, the model results show that wind–evaporation feedback dominates over cloud–radiation feedback for ISO propagation; this is in contrast to our estimates using the newly available European Centre for Medium Range Weather Forecasts Interim reanalysis. Sensitivity experiments suggest that intraseasonal variability in the CFS model with the RAS scheme is highly sensitive to the parameterization of both the shallow convection and the convective rain evaporation and downdrafts. Removal of these components adversely affects the propagation characteristics and greatly reduces the amplitude of intraseasonal variability. Our results support the primary importance of the moisture preconditioning ahead of the ISO and the physical relationship between moisture and precipitation. For realistic ISO simulations, models need to represent these features appropriately.

Keywords Intraseasonal oscillation (ISO) · Moist static energy (MSE) budget · Moist and thermodynamic process · Wind–evaporation feedback · Cloud–radiation feedback · RH–precipitation relationship

K. P. Sooraj · K.-H. Seo (✉)
Department of Atmospheric Sciences, Pusan National University, Busan 609-734, South Korea
e-mail: khseo@pusan.ac.kr

Present Address:
K. P. Sooraj
Centre for Climate Change Research (CCCR), Indian Institute of Tropical Meteorology, Dr Homi Bhaba Road, Pashan, Pune 411008, India
e-mail: sooraj@tropmet.res.in

1 Introduction

The Madden–Julian Oscillation (MJO) is the most significant mode of intraseasonal variability in the tropics, as throughout the seasonal cycle, the tropics experience strong and coherent intraseasonal variations in wind and precipitation (Madden and Julian 1994). The MJO is predominantly confined to the equatorial region in boreal winter and spring. In contrast, the boreal summer time intraseasonal oscillation (BSISO) has a complex spatial structure and propagation pattern owing to the northward propagation of the thermal equator and interaction with the Asian

summer monsoon (e.g. Lau and Chan 1986; Annamalai and Slingo 2001; Kemball-Cook and Wang 2001; Seo et al. 2007). So for BSISO, eastward propagating convection anomalies along the equator coexist with northward propagating convection anomalies from the Indo-western Pacific to the landmasses of India and Southeast Asia, leading to active and break cycles in Asian summer monsoon. While the eastward propagation speed generally varies from 4 to 6 m s^{-1} (Zhang 2005), the poleward disturbances usually assume speeds ranging between 1 and 2 m s^{-1}, with higher speeds in that range typically occurring in the Asian longitudes.

Several theories have been suggested to explain the observed BSISO. Some studies (Webster 1983; Goswami and Shukla 1984) depict northward propagation as the result of a prevailing meridional gradient in moist static energy (the northern side becomes more unstable than the southern side). Lau and Peng (1990) suggested that convective feedback between monsoon flow and the equatorial MJO can trigger (in numerical experiments) westward propagating Rossby waves over the Indian monsoon region. The model study of Wang and Xie (1997) show that continuous northwestward propagating Rossby waves (tilted convection front) are seen to emanate from an equatorial Kelvin wave as it crosses the maritime continent, creating northward moving rain bands. Jiang et al. (2004) proposed the importance of barotropic vorticity for independent poleward propagating events (i.e., without eastward component) over the Indian longitudes. According to them, the vertical shear mechanism is responsible for such barotropic vorticity occurring north of the convective maximum. Besides these internal processes, local air–sea interaction also play a role in northward propagating ISO, as highlighted in various observational (Bhat et al. 2004; Vecchi and Harrison 2002; Sengupta et al. 2001) and modeling studies (Woolnough et al. 2001; Fu et al. 2003; Kemball-Cook et al. 2002). A recent study by Chou and Hsueh (2010) provides a comprehensive summary of the current understanding on the northward propagation of ISO.

It appears that the northward propagating modes originate from the same disturbance as the eastward propagating MJO (e.g. Wang and Rui 1990; Lawrence and Webster 2002); however, this is still controversial in some quarters (Jiang et al. 2004; Lin et al. 2008). We refer to these two modes collectively as the BSISO (for brevity, we may simply call it as the ISO as well) and treat them together as one phenomenon.

In tropical dynamics, a dominant feature is the interaction of the large-scale circulation with moist processes arising on small scales. Previously, Neelin and Held (1987) formulated a method based on the vertically integrated moist static energy (MSE) budget in order to gain further insights into this interaction. Following this, several observational studies examined the MSE and energy budgets (Kemball-Cook and Weare 2001; Trenberth and Stephaniak 2003; Back and Bretherton 2006) for understanding the ISO and other tropical disturbances. In particular, Kemball-Cook and Weare (2001) suggested that MSE is a useful diagnostic tool for examining the recharge-discharge paradigm for tropical intraseasonal disturbances. In other words, a buildup of column MSE occurs before the initiation of ISO deep convection (Johnson et al. 1999; Kikuchi and Takayabu 2004; Kiladis et al. 2005; Benedict and Randall 2007), and then, the column integrated MSE decreases during periods of strong convective and stratiform heating. Observational studies (Neelin and Held 1987; Back and Bretherton 2006) suggest that the large-scale circulations in the western Pacific and Indian Ocean (IO), where the mean vertical profile is robustly determined by deep convection, export MSE in the mean. In these regions, the ISO amplitude is the strongest and MSE discharge appears to be enhanced during the deep convective and stratiform phases of the ISO (Johnson et al. 1999; Kiladis et al. 2005).

Recent modeling studies have extensively used this MSE diagnostic to better understand the instability mechanism responsible for maintaining intraseasonal anomalies against dissipation (Maloney 2009; Boos and Kuang 2010; and Andersen and Kuang 2012). The intraseasonal budget in the Community Atmosphere Model version 3 (CAM3) with a realistic basic state showed the importance of horizontal advection and latent heat flux in regulating the MSE discharge-recharge cycle (Maloney 2009). Andersen and Kuang (2012) also observed the dominance of horizontal advection in their MSE budget. However, in contrast to Maloney (2009), they observed that the latent heat flux has only a small budget contribution. Other MSE budget studies, through carefully designed sensitivity experiments, came to the conclusion that MSE discharge during the MJO convection may be modified by cloud–radiation feedback and wind–evaporation feedback, which could reduce or change the sign of the MSE tendency (e.g. Raymond 2001; Lin and Mapes 2004; Peters and Bretherton 2006; Sugiyama 2009a, b; Boos and Kuang 2010). For example, Boos and Kuang (2010) using MSE diagnostics and model sensitivity tests suggested that wind–evaporation feedback regulates the MSE tendencies.

A comprehensive MSE budget focusing on poleward propagating disturbances over the Asian monsoon regions has not been specifically addressed thus far, except for in a few studies (e.g. Boos and Kuang 2010; Ajayamohan et al. 2010). We intend to perform this diagnostic here in order to understand the instability mechanism associated with poleward propagating intraseasonal disturbances in a climate model.

Simulations of the ISO/MJO have been an area of great scientific interest; however, thus far, it seems to be a difficult

task for global models, and a diversity of opinions exists on the modeling of this phenomenon. One needs to understand the central issues that govern the structure, dynamics, and maintenance of this phenomenon. The uncertainties and shortcomings of ISO simulations can be attributed to deficiencies in relation to basic states, air–sea coupling, convective parameterizations, diabatic heating profile, and stratiform precipitation fraction (Slingo et al. 1996; Inness and Slingo 2003; Seo et al. 2007; Kiladis et al. 2009; Zhang and Hagos 2009; Seo and Wang 2010). Slingo et al. (1996) suggested that the details of the model convective parameterization were an important factor in the realism of their MJO simulations, and other studies have supported this conclusion (e.g. Wang and Schlesinger 1999; Lin et al. 2006). For example, Wang and Schlesinger (1999) found that a large relative humidity criterion in the convective parameterization is crucial for the amplification of the MJO.

Recently, there has been some progress in understanding the moist processes associated with the development and maintenance of intraseasonal disturbances. The following processes have emerged through various observational (Benedict and Randall 2007) and modeling studies (Zhang and Mu 2005; Boyle et al. 2008; Zhu et al. 2009; Fu and Wang 2009). Shallow cumulus and congestus precondition the atmosphere by moistening and warming the lower (and middle) troposphere, followed by the development of deep convection and moistening of the entire troposphere. Along with this deep convection, convective downdrafts tend to produce cold and dry outflow in the subcloud layer, which in turn modulates the future convection. Stratiform cloudiness then forms in the upper troposphere and the precipitation there falls into relatively dry lower levels, cooling the air through evaporation. Although downdrafts and evaporation cool and dry the lower troposphere in immediate proximity to the convection, studies indicate that they promote a cooler and moister mean tropical lower troposphere owing to weaker compensating subsidence away from the convection (Johnson 1976; Cheng 1989). The parameterization of convective precipitation evaporation and convective downdrafts has been shown to improve the simulation of convection by cumulus schemes (e.g. Kao and Ogura 1987; Maloney and Hartmann 2001). Recently, Straub et al. (2010) found that most of the global climate models exhibited a lack of low-level drying near the location of maximum rainfall and proposed this to be one of the main reasons for the failure of convectively coupled Kelvin waves in manifold global climate models. They attributed this to the deficient representation of shallow and convective downdrafts in global climate models. On similar lines, Seo et al. (2012) also studied the importance of shallow convection to convectively coupled Kelvin waves and concluded same. Given the importance of the aforementioned processes on the ISO life cycle, we investigate their impact on ISO simulation using NCEP climate forecast system (CFS) with a relaxed Arakawa Schubert scheme (RAS; Arakawa and Schubert 1974; Moorthi and Suarez 1999). In particular, using a suite of experiments, we examine the pivotal roles of the following apparently crucial processes: shallow convection and convective rain evaporation and downdrafts.

This study has two objectives. First, we explore the MSE budget in a coupled model (NCEP CFS with RAS scheme), so as to understand the model's ability in reproducing the moist and thermodynamic processes associated with the poleward moving BSISO disturbances. Second, we carry out sensitivity experiments to examine the important elements or components of the model physics that are crucial for the development, maintenance, and propagation of ISO disturbances. Our study is quite distinct from other similar analyses, because our analysis is based on a model that uses a more explicit representation of deep convection. Furthermore, the ISO in our model shows both eastward and poleward propagation. Stated otherwise, we use a coupled model with realistic boundary conditions that captures both the eastward and poleward propagating ISO components having amplitude and propagation speed similar to that of the observed ISO.

The structure of this paper is as follows. In Sect. 2, the model is described and experimental details are provided along with a description of the observations and reanalysis data set used. Mean state and ISO characteristics in the simulations are described in Sect. 3. In Sect. 4, intraseasonal MSE budget analysis is presented. The moistening process over India and surrounding seas is elucidated in Sect. 5. Section 6 examines the sensitivity of the CFS with the RAS scheme to shallow convection and to convective rain evaporation and downdrafts. Conclusions are presented in Sect. 7.

2 The model and data

2.1 The CFS model

This study uses the NCEP's coupled ocean–atmosphere CFS model. The atmospheric component of the CFS is the NCEP Global Forecast System model as of February 2003 (Moorthi et al. 2001). It adopts a spectral truncation of 62 waves (T62) in the horizontal (which is approximately 209 km) and a finite differencing in the vertical with 64 sigma layers. The oceanic component is the Geophysical Fluid Dynamics Laboratory (GFDL) Modular Ocean Model version 3 (MOM3, Pacanowski and Griffies 1998), which is a finite difference version of the ocean primitive equations under the assumptions of Boussinesq and hydrostatic approximations. The adopted domain for MOM3 in the CFS

is quasi-global, extending from 74°S to 64°N. The latitudinal resolution is 1/3° between 10°S and 10°N, gradually increasing through the subtropics until reaching a fixed value of 1° poleward of 30°S and 30°N. There are 40 layers in the vertical with 27 layers in the upper 400 m. The atmospheric and oceanic components are coupled once a day with no flux adjustment. For more details of the CFS model, the readers are referred to Saha et al. (2006).

2.2 The model simulations and experiments

First, a control run of the CFS (CTRL) is performed using the RAS cumulus parameterization scheme (Moorthi and Suarez 1999) to see whether this model simulates the characteristic ISO progression as explained in the introduction. Note that a previous study by Seo and Wang (2010) reported that the CFS simulation with RAS parameterization produced much improved boreal winter ISO. To investigate the important components or physical processes that are important to the ISO life cycle (as described in the introduction), a series of sensitive experiments is conducted by turning off the following components in the model: shallow convection (EXP1) and convective rain evaporation and downdrafts (EXP2). Additionally, to examine the impact of the deep convection scheme applied, a model run is performed (denoted as SAS) with a simplified Arakawa–Schubert cumulus parameterization scheme (Arakawa and Schubert 1974; Pan and Wu 1995). The summary of the experimental details is provided in Table 1.

Shallow convection is applied in the model to the atmospheric state where convective instability exists below approximately 700 hPa but no deep convection occurs; it is parameterized as an extension of the vertical diffusion scheme based on Tiedtke (1983). That is, the vertical mixing of heat and moisture within a convectively unstable layer is calculated with prescribed turbulence diffusivity. To evaluate this effect in the CFS model, shallow convection is turned off for EXP1. In relation to EXP2, no assumption is made for downdrafts and it can be either saturated or unsaturated (see Moorthi and Suarez, 1999). Note that EXP2 is performed by switching off both subroutines (related to convective downdrafts and convective rainfall evaporation) within the RAS cumulus parameterization scheme.

Table 1 Experimental details

Experiment details	Description	Convection scheme
CTRL	All physical process are allowed	RAS
EXP1	Shallow convection (Tiedtke 1983) turned off	RAS
EXP2	Convective downdrafts and subgrid-scale convective rainfall evaporation turned off	RAS
SAS	All physical process are allowed	SAS

These simulations were initialized from the observed analysis of January 1, 1984. For the simulations consisting of CTRL and SAS, 13-year simulations are conducted. For all the sensitivity tests (EXP1 and EXP2), 6-year simulations at standard model resolution are conducted. The initial condition for the atmosphere was taken from the NCEP/DOE Reanalysis-2 (Kanamitsu et al. 2002), and the initial condition for the ocean was from an NCEP global ocean data assimilation system (GODAS; Seo and Xue 2005).

2.2.1 Observations

The observational precipitation data used in this study is the daily precipitation from the Global Precipitation Climatology Project (GPCP, version 2.1, Huffman et al. 2001). We also use European Centre for Medium Range Weather Forecasts (ECMWF, Berrisford et al. 2009) Interim reanalysis data set (here after called reanalysis or ERA) for performing circulation and MSE budget diagnostics. The reanalysis product, based on a system that uses a new humidity analysis and improved model physics (Simmons et al. 2007), covers the data period of 1989–2009, and it is considered to accurately capture the tropical precipitation and the hydrological cycle. The horizontal resolution is 1.5° and there are 60 vertical levels. More details can be found in Simmons et al. (2007).

The daily anomalies for both the observations and simulations are calculated by removing the annual cycle, composed of the time mean and the first three harmonics. Then, Lanczos band pass filters (Duchon 1979) with 200 weights and retaining periods of 20–90 days are applied to the anomaly data sets covering all the seasons. Finally, daily data corresponding to the boreal summer season (May through October) are extracted for analysis.

3 Simulation of the mean state and intraseasonal characteristics

In this section, we demonstrate the ability of the model to simulate the basic state and ISO characteristics. This section ends by discussing the space–time evolution of ISO characteristics.

3.1 Basic state and ISO features

The Asian summer monsoon (ASM) consists of multiple regional heat sources or local maxima in rainfall (see Fig. 1a). Of these, the primary one is noted over the Indian subcontinent and the Bay of Bengal (BoB) between 15°N

and 25°N. The secondary heat zone is observed over the equatorial IO between the equator and 10°S and the third one is found over the warm waters of the tropical western Pacific. The CTRL simulation captures the locations of these regional centers, but the simulated intensities are stronger (Fig. 1b). For example, the rainfall over the eastern Arabian Sea, western peninsular Indian region, and equatorial IO is overestimated. Further, the model tends to generate a spurious double intertropical convergence zone (ITCZ) in the western Pacific, instead of the observed dominant northern ITCZ (Fig. 1a). The pattern correlation coefficient between the observed and simulated precipitation climatology over the ASM region (40°E–120°E, 20°S–30°N) is 0.8. The simulated precipitation climatology is comparable to that of other state-of-the-art coupled models, as shown in Sperber and Annamalai (2008).

The vertical shear in the mean zonal wind (see contour lines in Fig. 1) is shown to be critical for both northward and eastward propagation (Webster and Yang 1992; Wang and Xie 1997; Kemball-Cook et al. 2002; Jiang et al. 2004). This easterly vertical wind shear favors the emission of Rossby waves, as well as the eastward propagating equatorial waves by diabatic heating associated with the ISO (Wang and Xie 1997; Krishnan et al. 2000). Consistent with the simulated heating pattern, the simulation (see Fig. 1b) captures the observed spatial structure with an easterly shear north of 10°S over the IO and western Pacific, but the shear is somewhat weaker than observed (Fig. 1a).

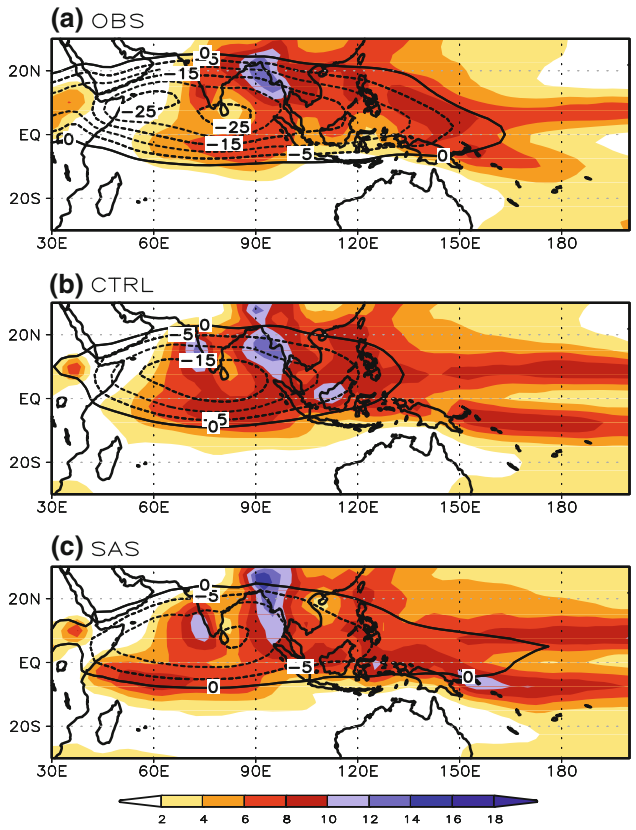

Fig. 1 Summer (May to October) mean rainfall (mm day^{-1}, *shaded*) and zonal wind shear (m s^{-1}, *contours*) for **a** OBS (rainfall from GPCP), **b** CTRL, and **c** SAS

In Fig. 1, we have also displayed the model mean state from SAS simulation. In general, the basic state in diabatic heating and in the first internal baroclinic mode (easterly shear) over the ASM region shows good correspondence with that of CTRL (see Fig. 1b, c). The pattern correlation coefficient between the two simulated precipitation climatology over the ASM region is 0.86. However the details of the structure differ regionally. For example, over the eastern equatorial IO and western north Pacific, SAS produces precipitation closer to observations than CTRL. On the other hand, over the Indian landmass, CTRL captures comparable precipitation to observation than SAS. Further, the eastward extension of the vertical shear (up to 170°E) is more realistic in SAS than in CTRL, but its overall magnitude is weaker than in CTRL. Additional examination using the mean sea surface temperature (figure not shown) distribution demonstrates that the CTRL simulation has a cold bias of approximately 1 °C along the equatorial Pacific, acting to suppress ISO activity and its propagation. But, this bias is comparatively smaller in SAS. However, our subsequent results will show that the simulations of intraseasonal variability are vastly different for SAS and CTRL. It should be noted here that the intention of the present research is not to appraise the superiority of one scheme over the other in simulating climatology. We are, instead, interested in elucidating the relevant physical and dynamical processes associated with the BSISO, as will be made clear in the following sections.

The monsoon convection over the ASM domain spends more time near the equator and the poleward limit of its propagation than in intermediate latitudes. This explains the time-mean low-level convergence zones near the equator and 20°N, as described earlier (Fig. 1a). Moreover, the observed spatial distribution of intraseasonal variance in precipitation shows higher variance over the oceanic region compared to over land, which is true for both hemispheres, even in regions where the climatological mean precipitation is larger over land than ocean (Sobel et al. 2008). Accordingly, the observations exhibit (figure not shown) larger variance over two regions: one over the equatorial eastern IO region (75°E–100°E, 10°S–5°N, denoted as EIO) and the other over a relatively smaller region confined to the BoB (85°E–95°E, 10°N–20°N). The simulations capture both these local variance maxima (figures not shown). We consider the time series of precipitation anomalies averaged over the larger region (EIO) as the base time series, and the regression coefficients of

precipitation and other variables are estimated against this time series. Unless otherwise specified, we use the same procedure for the ISO diagnostics (for both the model and the observations) throughout this paper.

Now, we present the propagation characteristics (both the equatorial eastward propagation and the northward propagation) over the Indian monsoon region, constructed from the regression analysis. First, we look at the equatorial component of the ISO in the model and compare it against the observations. For the observations, regression analysis (Fig. 2a) confirms the genesis of the ISO over the equatorial western IO, with 850-hPa easterly anomalies over the western Pacific and local maxima in precipitation over the equatorial EIO. It shows coherent eastward propagation into the western Pacific (after 10 days), where westerly anomalies ensue soon afterwards. As the rainfall anomalies reach the central equatorial Pacific (after 20 days), the western Pacific shows suppressed convection. The CTRL simulation (Fig. 2b) depicts similar observed features, with an apparent low-level convergence flow to the east of the deep convection. The observed lag ($\sim$5 days) between zonal wind and precipitation (the zonal wind anomaly lagging behind the precipitation) is also simulated well. Thus, the observed phase relationship between positive convection and wind anomalies is well maintained by the CTRL simulation, with the model convection tending to be shifted out of the center of the easterlies. However, there are problems in the eastward extension of the convection into the central equatorial Pacific and in the in situ amplitude (which is slightly weaker). Moreover, in the simulation, the propagation is slightly slower over the IO than in the observations. On the other hand, SAS shows (Fig. 2c) reduced easterly anomalies to the east of the convective maximum, thus producing weaker wind convergence. Hence, it depicts total collapse of the MJO propagation with a stationary pattern over the western to central Pacific sector. This lack of coherent eastward propagation from the IO to the Pacific has also been noticed in the CFS T62 simulation with SAS scheme (Seo et al. 2005) and in other simulations (e.g. Slingo et al. 1996; Inness and Slingo 2003; Sperber et al. 2005).

Next, we present the space–time spectral analysis in order to demonstrate the dominant peak representing the propagating disturbances in the model. This analysis is particularly useful for the study of zonally propagating waves; it decomposes a field into wavenumber and frequency components for eastward and westward propagating waves (Wheeler and Kiladis 1999). Herein, wavenumber-frequency spectra are calculated for observed and simulated precipitation data using the methodology described in Wheeler and Kiladis (1999). We first removed the annual cycle composed of the time mean and first three harmonics. The data are averaged over the equatorial

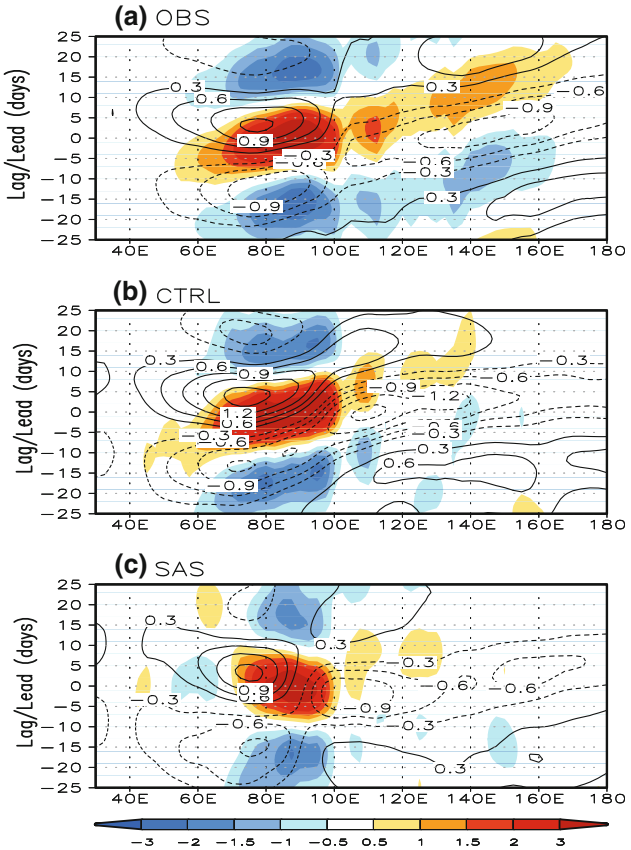

Fig. 2 Lag-longitude diagrams (for boreal summer ISO) of regressed rainfall (mm day^{-1}, *shaded*) and 850 hPa zonal wind (m s^{-1}, *contours*) anomalies along the equator from **a** OBS, **b** CTRL, and **c** SAS. Regression is with respect to the base time series of rainfall averaged over EIO region (75°E–100°E, 10°S–5°N)

region, separated by individual years. Only the summer season is used here in computing the spectra, and the wavenumber-frequency is computed for each year and then averaged across the years.

The observed precipitation spectrum (Fig. 3a) is dominated by eastward periods of 30–80 days, with power concentrated at wavenumbers 1–3 (e.g. Salby and Hendon 1994). The maximum value of the spectrum occurs near periods of 40–50 days and wavenumber 1. The CTRL (Fig. 3b) simulation has power concentrated between wavenumbers 1 and 3, with a spectral peak occurring near periods of 50–70 days, and hence, it tends to have higher power at slightly lower frequencies than observed. However, SAS (Fig. 3c) has not reasonably captured the observed peak; instead, its variance maximum is shifted towards lower frequencies (100–200 days). Interestingly, it shows a heightened westward convective precipitation at wavenumber 3 at ISO periods. These spatial and temporal scales and the corresponding spectral peak are not present either in observations or in CTRL. In short, both the model (CTRL simulation) and observations show distinct eastward

propagation during boreal summer, similar to the boreal winter period (Lawrence and Webster 2002; Wheeler and Hendon 2004). As per the observational evidence, it shows a weaker eastward propagating precipitation signal in northern summer than its counterpart in northern winter (Wheeler and Hendon 2004; Zhang and Dong 2004). Consequently, it is more difficult to simulate the eastward component during boreal summer than in boreal winter. The problems in the CFS, such as the eastward extension of convection into the central equatorial Pacific and weak amplitude over there, may be partly related to the nature of the seasonality of the observed ISO variability.

Figure 4 shows the time-latitude precipitation (shaded) regression maps, along with 850 hPa zonal wind anomalies, for the observation and CTRL simulation. The model (Fig. 4b) almost captures the observed (Fig. 4a) northward migration of precipitation anomalies over the Indian monsoon region, with precipitation leading zonal wind by 5 days. The phase relationship is well captured, with westerly anomalies existing under deep-precipitating ISO convection along the equator, while an easterly anomaly develops to the north of this convection. However, there are some differences as well. The simulated rate of poleward propagation is slower (by approximately 1 pentad, see the dashed lines in Fig. 4a, b) than in the real world. Further, the simulated strength of zonal wind anomalies is larger compared to the observations. However, SAS (see Fig. 4c) clearly shows considerably reduced propagation characteristics, compared to CTRL and the observations. The poleward propagating anomalies decrease strongly both in amplitude and in the meridional distance they transit after a lag of 15 days (see the dashed lines in Fig. 4c).

Wang and Rui (1990) found that approximately half of poleward propagating ISO events in Asia occurred concurrently with eastward propagation. However, Lawrence and Webster (2002) estimated this fraction to be higher (75 %). Despite the discrepancy between their studies, a

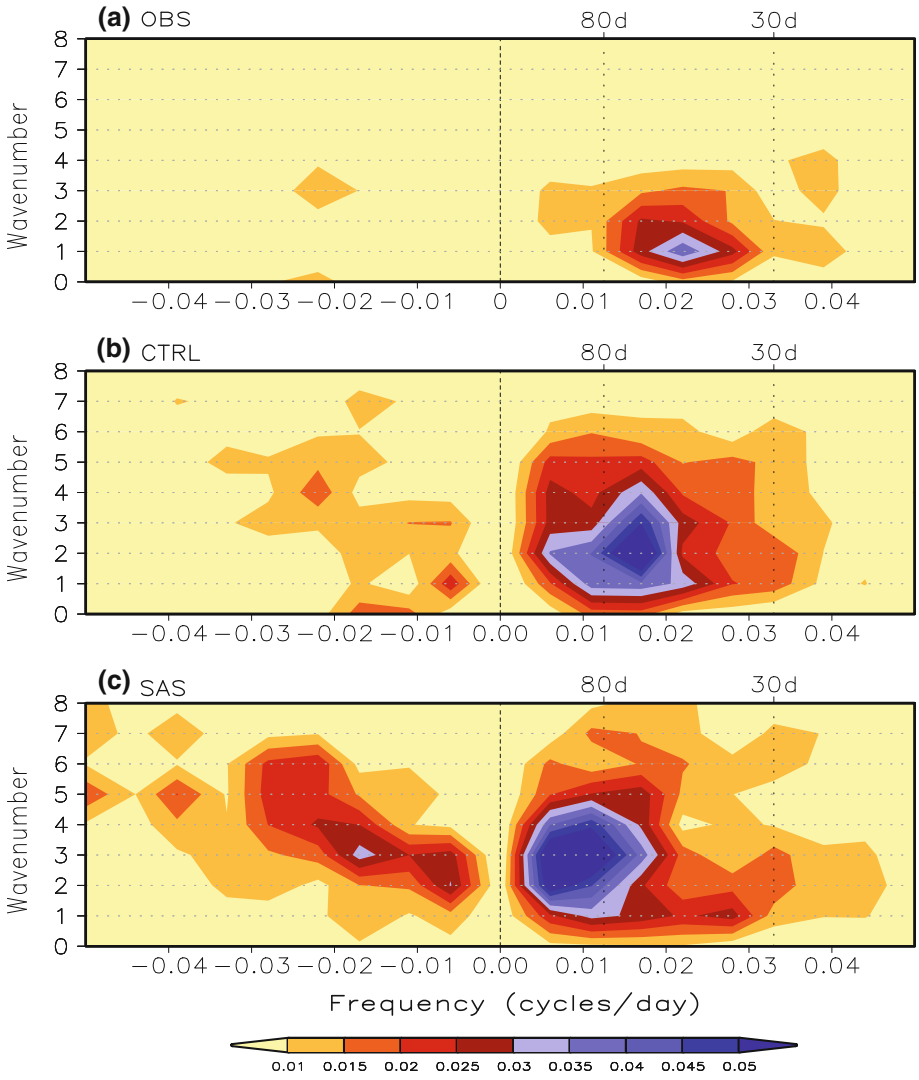

Fig. 3 Wavenumber-frequency spectra of equatorial (over EIO region) rainfall during the boreal summer season for **a** OBS, **b** CTRL, and **c** SAS. Individual May to October spectra were calculated for each year, and then averaged over all years of data. Only the climatological seasonal cycle was removed before calculation of the spectra. The units for spectrum are $mm^2\ day^{-2}$ per frequency interval per wave number interval. The bandwidth is $(180\ days)^{-1}$

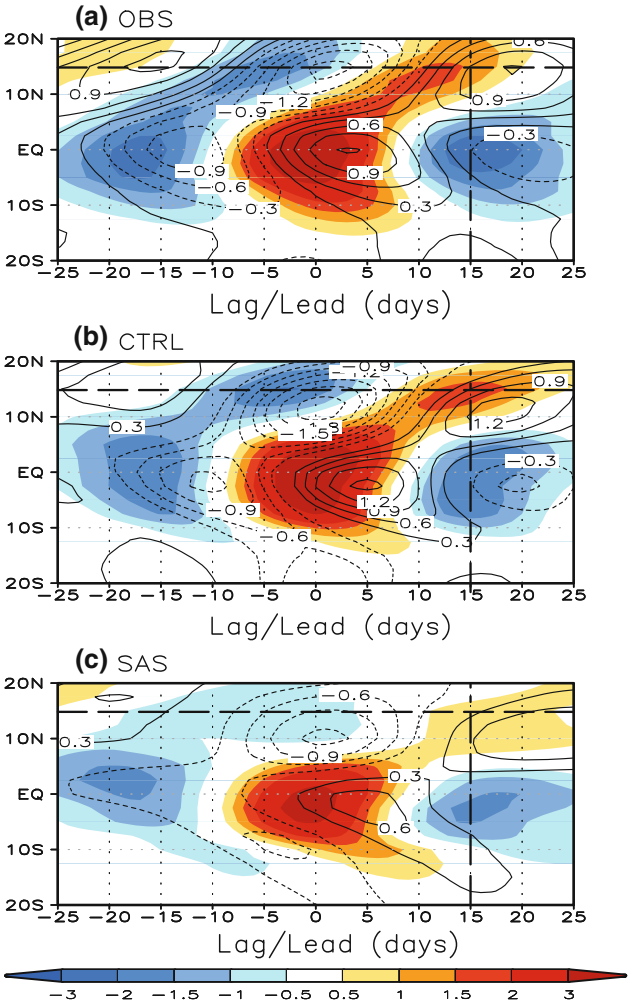

Fig. 4 Lag-latitude diagrams (for boreal summer ISO) of regressed rainfall (mm day^{-1}, *shaded*) and 850 hPa zonal wind (m s^{-1}, *contours*) anomalies averaged over 70°E–100°E from **a** OBS, **b** CTRL, and **c** SAS. Regression is with respect to the base time series of rainfall averaged over EIO region. Dashed lines are for comparing the propagation characteristics against the observation

recent study by Sperber and Annamalai (2008) on the BSISO characteristics in CMIP3 coupled models pointed out that a realistic simulation of the equatorial component of the ISO is a necessary criterion for simulating the subsequent poleward migration over the Indian monsoon region. This argument followed from their observations that almost all CMIP3 models (with various degrees of fidelity) simulated the equatorial component over the IO with considerable intensity of convection. Combined interpretations of the results from CTRL (realistic simulation of both eastward and northward propagating components; Figs. 2b, 4b) and SAS (its failure to capture both of these components, Figs. 2c, 4c) further substantiate their findings. The suggestion here is that this model (with the RAS convection scheme) is capable of capturing the basic elements of the BSISO over the ASM region.

The above disparities in the ISO characteristics of two simulations (CTRL and SAS) appear to stem from the different treatment of deep convective clouds. The SAS scheme considers only simple deepest cloud (an updraft and downdraft couplet) and moisture detrainment at the cloud top, whereas RAS considers a spectrum of cloud types with different heights and entrainment rates and allows convective detrainment at various levels. So, these differences result in different precipitation patterns and vertical heating and moistening profiles (Byun and Hong 2004). A previous study by Seo and Wang (2010) also found that the CFS simulation with RAS parameterization outperforms that with SAS parameterization, in simulating the eastward propagating boreal winter ISO. They argued that a top-heavy vertical heating profile arising from convective detrainment of moisture to the environment and stratiform precipitation play a critical role in the improvement of the ISO simulation, by generating eddy available potential energy. In a subsequent study, using the same model configurations (with RAS scheme), Seo et al. (2012) further showed that the removal of convective detrainment (refer to sensitivity experiment EXP2 of their paper) results in greatest reduction of convectively coupled Kelvin waves.

3.2 Space–time evolution of ISO

Here, we look into the horizontal structure of the lead/lag relationship shown in Fig. 4 for more clarity. Further, in order to simulate the timing of the active and break phases of the ASM, it is desirable that a climate model be capable of simulating the observed variability realistically. In Fig. 5, we show the lead/lag evolution of precipitation and low-level wind anomalies from the CTRL simulation. As shown in other studies (Lau and Peng 1990; Wang and Rui 1990; Annamalai and Slingo 2001; Ajayamohan and Goswami 2007), typical observed characteristics captured by the CTRL simulation can be described as follows. Initiation of the ISO occurs over the western to central IO region at day −10 (see Fig. 5a, i). This is followed by amplification over the EIO (at day 0, see Fig. 5b, j), moving eastward as time progresses. In response to the moist conditions over the equatorial IO, low-level cyclonic anomalies are noticed. On the other hand, there is development and eastward extension of negative rainfall anomalies over the northern IO with resultant low-level anticyclonic circulation anomalies (see Fig. 5b, j). Further, possibly because of the interaction of these circulation anomalies, the largest easterly wind anomalies are observed over the northern Arabian Sea at day 0. Over the EIO, the rainfall bifurcates towards northern and southern latitudes (at day 5, see Fig. 5c, k) as Rossby waves are emitted. The northern lobe propagates steadily northward,

while the southern one is fully diminished by day 15 (see Fig. 5d, l). However, the SAS simulation with weak rainfall and circulation anomalies (see Fig. 5e–h) failed to capture these robust features of the internal processes, re-emphasizing the impact of deep convection on the robustness of ISO characteristics. In particular, the coherent and persistent eastward propagating rainfall anomaly and its subsequent bifurcation over the EIO are totally absent in the simulation (see Fig. 5g). In the observations (at day 15, see Fig. 5l), positive rainfall anomalies are oriented along a northwest-southeast diagonal stretching from western central India to the equatorial western Pacific. One obvious limitation in the CTRL simulation is its failure to capture this slanted precipitation band.

In summary, the CFS model with the RAS scheme simulates robust eastward and northward propagating BSISO in a comparable manner to the observation. However, the intraseasonal variability in the model (CTRL simulation) exhibits some features that differ from the observed ISO in the following ways. Firstly, there is a problem in the eastward extension of the equatorial convection into the central equatorial Pacific (see Fig. 2a, b). Secondly, the spatial structure of precipitation anomalies associated with northward propagation exhibits some biases relative to observations (see Fig. 5). Lastly, the frequency-wave spectrum of model precipitation is redder than the observed one (see Fig. 3a, b), a common problem in many global models that exhibit strong ISO variability (e.g. Zhang et al. 2006).

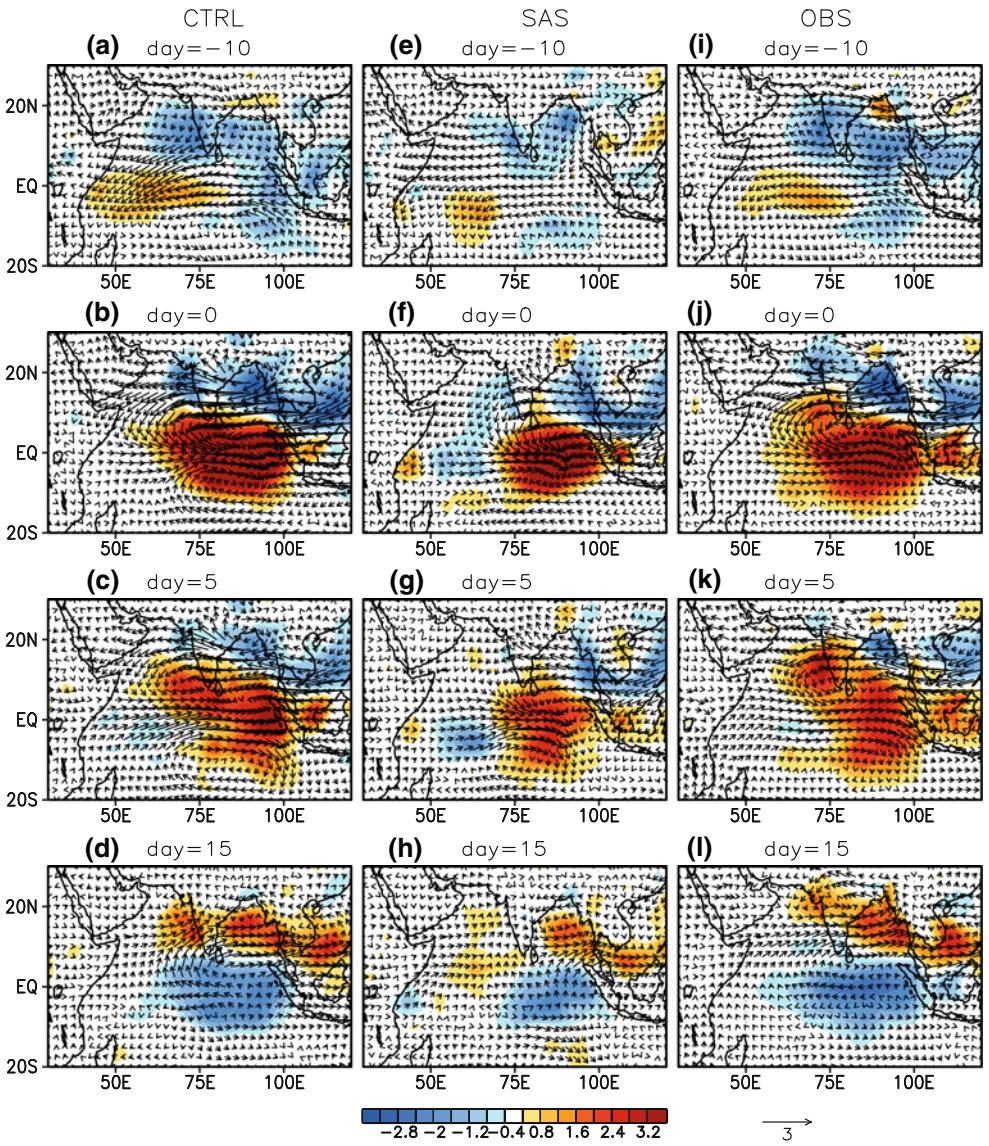

Fig. 5 Maps of regressed rainfall (mm day^{-1}, *shaded*) and 850 hPa wind (m s^{-1}) anomalies, showing the lead/lag evolution in boreal summer ISO. Regression is with respect to the base time series of rainfall averaged over EIO region. The left panel is from the CTRL simulation, while the central and right panel is from SAS and OBS, respectively

However, the realistic propagation characteristics, amplitude, and phase relationship that characterize the ISO (see Fig. 4a, b) suggest that this model captures some of the essential features of the observed ISO. Thus, examining the model intraseasonal MSE budget (in the next section) and the subsequent analysis based on sensitivity experiments (in Sect. 6) should be useful exercises.

4 Intraseasonal MSE budget diagnostics

It has been suggested that the northward propagation of the BSISO convection is a result of the systematic interaction of convection, surface dynamics, thermodynamics, and radiation (e.g. Kemball-Cook and Wang 2001). Here, we analyze the MSE budget for a detailed understanding of the moist and thermodynamic processes associated with the ISO disturbances. This diagnostic investigates the phase (lead/lag) relationship of different components of the MSE budget (horizontal advection, vertical advection, surface fluxes, and radiative heating) with respect to the BSISO convection. Subsequently, this can give insight into the effect of various processes in contributing to the destabilization and propagation of the ISO. MSE is defined as $m = c_pT + Lq + gz$, where c_p is the specific heat at constant pressure, T temperature, z height, g the gravitational acceleration, L the latent heat of vaporization at 0 °C and q the specific humidity (for more details on MSE budget, see Neelin and Held 1987). The vertically integrated MSE budget can be written as follows:

$$\overline{\frac{\partial m}{\partial t}} = -\overline{\vec{V}\cdot\nabla m} - \overline{\omega\frac{\partial m}{\partial p}} + LH + SH + \overline{LW} + \overline{SW} \qquad (1)$$

where $\vec{V}$ is the horizontal velocity vector, ω is the vertical pressure velocity and the overbar denotes the vertical integral running from the surface to 100 hPa. The first two terms of the RHS of (1) denote horizontal and vertical advection. The third and fourth terms in the RHS of (1) represent surface turbulent heat fluxes (sum of latent and sensible fluxes), while the rest of the terms denote radiative (longwave, $\overline{LW'}$ and shortwave, $\overline{SW}$) fluxes. The conventions are that negative (positive) values of longwave and shortwave radiation indicate cooling (warming) in the atmospheric column. Also, MSE advection into the column is positive and dry advection is negative. Of interest here are intraseasonal time scale variations in the vertically-integrated MSE budget and so the terms in Eq. (1) are band-pass filtered (20–90 days) for further analysis. The horizontal structure of these components is presented below.

4.1 Horizontal structure

We start our budget analysis by showing the lead/lag spatial map of vertically integrated MSE anomalies (20–90 day bandpass filtered), as shown in Fig. 6. Also shown are the corresponding distributions in moisture anomalies (shading). At first, it shows a strong similarity between the behavior of MSE and moisture, indicating that in the model (CTRL simulation), the variations in MSE on ISO time scales are mainly governed by moisture variations. Consistent with this, recent studies (Raymond and Fuchs 2009; Sugiyama 2009a; Boos and Kuang 2010) also suggest that the ISO is regulated by process controlling the tropospheric moisture field, under the assumption of weak tropical temperature gradients (Sobel et al. 2001).

Both MSE and moisture show slow northward propagation patterns, similar to that of the precipitation anomalies (see Fig. 5a–d). Therefore, in general, the evolution of their geographical distribution is approximately similar to that of the precipitation anomalies; this is in agreement with the documented strong relationship between precipitation and column water (e.g. Bretherton et al. 2004). However, a close look at the regression plots at day 0 and day 5 (see Fig. 6b, c) shows the poleward intrusion of enhanced MSE and moisture anomalies over the IO (especially over the Arabian Seas), slightly ahead of the enhanced rainfall anomalies (Fig. 5b, c). By day 15, these MSE anomalies have migrated as far as 30°N (see Fig. 6d). This poleward intrusion of moisture anomalies ahead of rainfall anomalies possibly illustrates the effect of moist Rossby waves, emanated due to the equatorial eastward extension of positive rainfall anomalies into the western Pacific. The continuous emanation of moist Rossby waves from the equatorial convection and their subsequent trapping in the ASM region by the mean easterly vertical shear, likely promote the poleward migration of BSISO anomalies (Wang and Xie 1997; Sperber and Annamalai 2008). This basic hypothesis seems to work well here in the CFS model.

In order to explore the internal moist-thermodynamic process leading to the poleward propagation characteristics, in Fig. 7, we present the individual terms of the MSE budget together with the residual term (all are regressed maps). In this figure, latent and sensible heat fluxes are combined because the latter is an order of magnitude smaller than the former. The residual is generally smaller compared to the leading MSE tendency terms, allowing us to have some confidence in our MSE diagnostics and subsequent inferences. The model budget estimates show a positive MSE tendency in advance of rainfall and a negative tendency during and after rainfall (Fig. 7a). This implies a large build-up or recharge of MSE (Kemball-Cook and Weare 2001) prior to the enhanced convection, for example, over the equatorial IO. This is followed by a discharge of MSE. These results are similar to the observed (Kiranmayi and Maloney 2011) and model (Maloney 2009; Boos and Kuang 2010; Andersen and Kuang 2012) results based upon the intraseasonal MSE budgets.

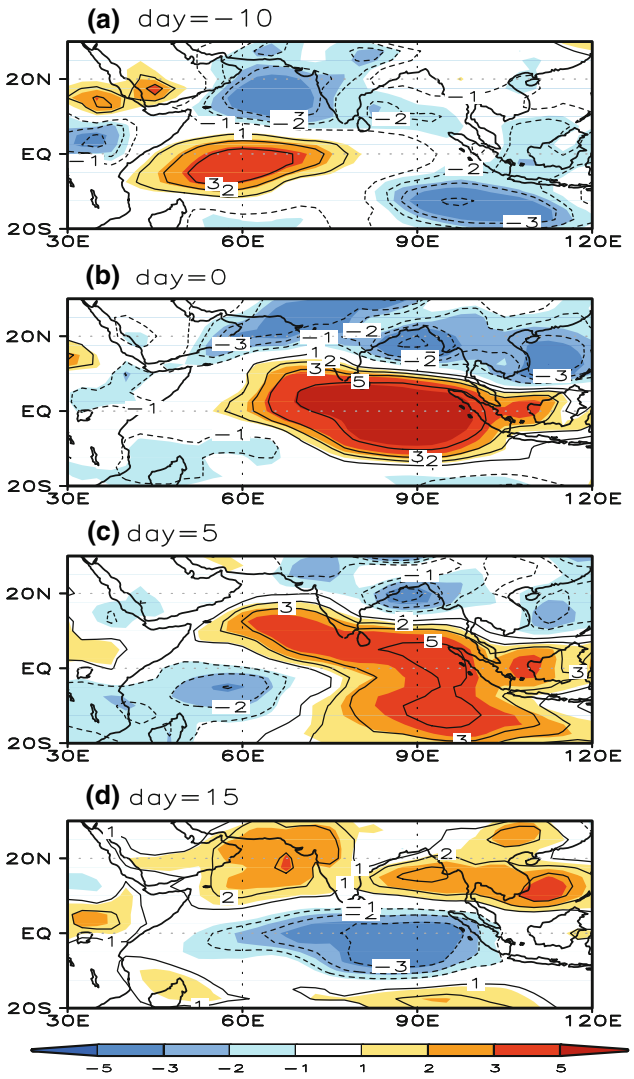

Fig. 6 Maps of regressed moisture ($\times 10^6$ J m^{-2} units, *shaded*) and MSE ($\times 10^6$ J m^{-2} units, *contours*) anomalies, showing the lead/lag evolution in boreal summer ISO, from the CTRL simulation. Both are vertically integrated from the surface to 100 hPa. Note that moisture anomalies are multiplied with latent heat of vaporization (L) for direct comparison with anomalous MSE. Regression is with respect to the base time series of rainfall averaged over EIO region

The role of various budget components in maintaining/dissipating the MSE anomaly as well as in promoting/retarding the propagation characteristics can be described in the following way. Both the horizontal and vertical advection terms ($-\overrightarrow{V'}\cdot\nabla m'$ and $-\overline{\omega'\frac{\partial m'}{\partial p}}$, Fig. 7b, c) are large and positive before the ISO rainfall peaks (say over 10°N–20°N, India/BoB region at lag 0) and are strong and negative after that. Again, both are more in phase with the MSE tendency than with precipitation anomalies, thus contributing to poleward propagation, with dominant contribution from horizontal advection. More details about this aspect are provided in Sect. 4b. Both further act as a sink of column MSE in the convective region. The radiative ($\overline{LW'}$ and $\overline{SW}$, see Fig. 7d, e) and surface turbulent ($LH' + SH'$, Fig. 7f) heat fluxes show positive covariance with precipitation. So their role is to enhance the MSE anomalies over the convective region, contributing equally to the maintenance of the MSE disturbances and thus balancing the sinks owing to horizontal and vertical advection (see Fig. 7b, c). On the other hand, both heat fluxes (turbulent and radiative) show an out of phase relation with the MSE propagation tendency, thus acting against MSE recharge. This indicates that both heat fluxes appear to oppose the poleward propagation tendency, with the turbulent component of heat fluxes dominating the other one (radiative).

The observational analysis of Waliser (1996) suggests that both the turbulent and radiative components may be of comparable magnitude, while Hendon and Glick (1997) suggest that their relative importance depends upon the location. Other model studies also suggest that surface turbulent heat fluxes have a prominent role in regulating ISO-related precipitation (e.g. Maloney and Sobel 2004; Maloney 2009; Boos and Kuang 2010). In particular, in their study based on boreal winter ISOs, Maloney (2009) used a model (in CAM3) based MSE budget to show that anomalous turbulent surface heat fluxes oppose the MSE tendency. Recently, Boos and Kuang (2010) also draw similar conclusions for the poleward propagating disturbances in their cloud resolving model, using MSE diagnostics and model sensitivity tests.

We perform similar MSE budget diagnostics (figures from reanalysis are not shown here for brevity) using the reanalysis for comparison against the budget estimates derived from the model. The budget estimates are calculated following the formulation in (1), but with the exception that radiative flux components are defined as the difference between the surface and top of the atmosphere fluxes. A substantial residual, as large as the tendency, exists in the reanalysis. Kiranmayi and Maloney (2011) also reported similar intraseasonal (for boreal winter ISOs) budget residuals in the reanalysis. They attributed this to the missing moistening source in the reanalysis model ahead of the MJO convection. Although the reanalysis is dissimilar to the observations and is constrained by errors in the moist physics, we use this data set for comparison as it represents a state-of-the-art attempt to reproduce realistic features on a global scale.

Many aspects of the reanalysis budget commonly resemble model (CTRL simulation) MSE estimates, with dominant contributions from horizontal advection in increasing (decreasing) column MSE before (after) an ISO rainfall peak. In addition, the surface turbulent heat and radiative heat fluxes contribute to the maintenance of MSE anomalies, with the latter dominating over the former. In

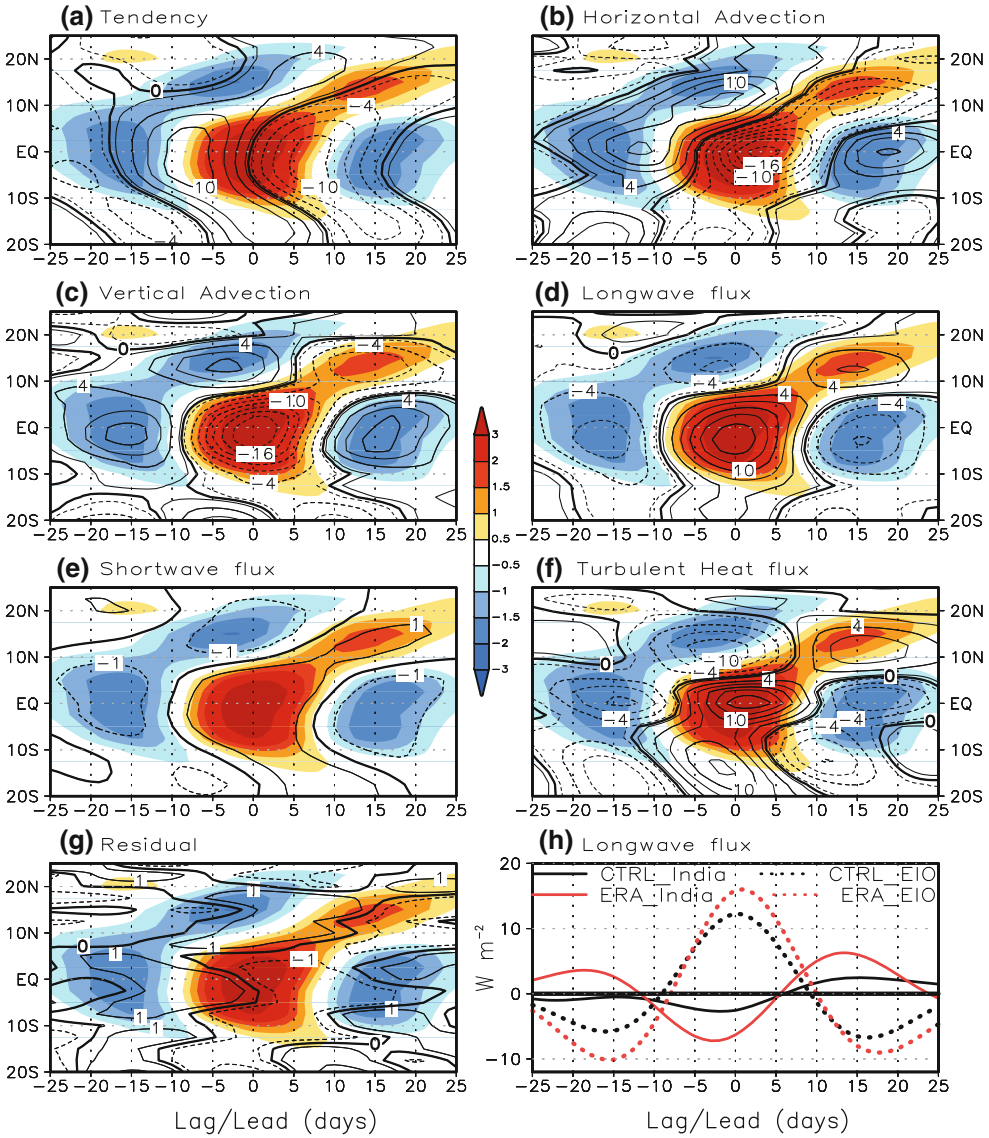

Fig. 7 Lag-latitude diagrams of regressed anomalies of intraseasonal MSE budget terms (vertically integrated) averaged over 70°E–100°E, from CTRL simulation. **a** MSE tendency, **b** horizontal MSE advection, **c** vertical advection, **d** longwave radiation, **e** shortwave radiation, **f** surface turbulent heat flux, and **g** residual. Regressed rainfall (mm day^{-1}) anomalies are shown in shading and budget terms in contours. First solid (*dashed*) contour of all MSE budget terms is 1 (−1) W m^{-2} and contour interval is 3 (−3) W m^{-2}. In **h** regressed anomalies of longwave radiative flux (W m^{-2}) over the EIO (denoted by *dotted lines*) and India/BoB regions (denoted by *thin lines*) are plotted. Reanalysis radiation fluxes are shown in *red*, while fluxes from CTRL are in *black*. Regression is with respect to the base time series of rainfall averaged over EIO region

contrast, in the model (CTRL simulation), both components contribute equally to destabilize the ISO anomalies. Again in the reanalysis, both flux components slow the discharge of column MSE as it is in positive covariance with precipitation, with a relatively larger contribution from the net radiative flux (especially the longwave component). However, on the contrary, the model estimates show less contribution from longwave fluxes than from surface turbulent heat fluxes. Specifically, over the India/BoB region (at lead 0), the longwave estimates in the model are approximately one-half of the amplitude observed in the reanalysis, resulting in an equivalent reduction in the model net radiation flux. Further, in the model, the surface turbulent heat fluxes are relatively large, both in the context of maintaining MSE anomalies and retarding its propagation. For example, over the regression base point (EIO, at lead 0), turbulent heat flux estimates in the model MSE budget are approximately twice those from the reanalysis. Furthermore, the corresponding zonal wind anomalies in the model are larger (about twice) compared to the reanalysis (see Fig. 4a, b). As per the wind induced surface heat exchange (WISHE, Emanuel 1987) argument,

the changes in wind speed across a convective disturbance are assumed to dominate changes in latent heat flux. So, it possibly implies that in the model, latent heat fluxes are largely determined by zonal wind anomalies.

The MSE budget results from the reanalysis imply that the net radiation flux (through longwave radiation) may play some important role in controlling the poleward propagation characteristics. Earlier, Neelin and Held (1987) suggested that the net radiative forcing at the top of the atmosphere is directly proportional to the low-level divergence. Thus, a detailed inspection of the radiation flux components will give more insight into the relationship between cloud–radiative feedbacks and circulation dynamics. Figure 7h shows the temporal evolution of the regressed anomalies of longwave radiation flux over the India/BoB region, from both the model and reanalysis budget estimates. The evolution over the EIO is also shown for better interpretation. We here display only longwave flux as it dominantly contribute to net radiation fluxes (figure not shown). Over the India/BoB region, the reanalysis show radiative cooling (red line) from day −12 onwards and this is expected to influence low-level circulation anomalies, which in turn amplify the negative rainfall anomalies (Neelin and Held 1987). This cooling dissipates slowly after day 5. Over the EIO region (red dotted line), there is an anomalous simultaneous radiative warming that starts growing from day −8 onwards, prevailing until day 10. This simultaneous evolution of heating and cooling signatures over the two domains implies a differential radiation flux across the latitude. In the model, the cooling (relatively smaller values) over the India/BoB region starts at a slightly earlier time and becomes dissipated after day 5 (black thin line). The anomalous radiative warming (over the EIO) grows from day −9 to day 0 (weaker warming compared to reanalysis) and dissipates by day 10 (black dotted line). Associated with this warming, the regional Hadley circulation will be modified (Goswami 2005), with an anomalous ascending motion over the equatorial IO and an anomalous descending motion over the India/BoB region. This follows from thermodynamic energy considerations, which imply that increased radiative cooling over the India/BoB region should be compensated by adiabatic descent (see Holton 1982) that is achieved here through local Hadley circulation. Previous studies have also suggested that convective variability between the EIO and the Indian subcontinent is linked through the regional Hadley cell (Sikka and Gadgil 1980; Krishnan et al. 2000). In addition, Raymond (2000) showed, using a modeling study, that the simulated Hadley circulation is sensitive to the cloud–radiation interaction. So here the results from the reanalysis indicate that cloud–radiation feedbacks are significant in maintaining the suppressed phase or break monsoon condition over the India/BoB region. Therefore, based on all these evidences, our interpretation is that cloud–radiation feedbacks are also important in regulating poleward propagation through the role of differential radiation flux in anchoring the local Hadley circulation. However, in the CFS, longwave radiative fluxes are not so vitally important in controlling the propagation characteristics, as we saw earlier. Given the importance of radiative fluxes as a retarding factor, their modest values deserve careful attention on the cloud–radiative feedback process operating in the model.

Owing to the relative phases of the various budget components, in the model it appears that propagation tendencies in MSE anomalies are primarily driven by horizontal advection. We will now focus our attention on this term to gain further insight into ISO propagation mechanisms (in Sects. 4b, 5).

4.2 Vertical structure of advective tendencies

Having identified the importance of horizontal advection in the MSE budget for ISO propagation characteristics, we now examine its vertical structure for further clarity. Figure 8 shows the regressed anomalies of the horizontal advection component of the MSE derived from the model, for a complete ISO cycle. Additionally, we look at the role of the vertical advection term (Fig. 9) for understanding its relative importance. The anomalous values of rainfall (see Fig. 8) and convective available potential energy (CAPE, see Fig. 9) are also displayed at the bottom of each panel for better illustration. In both figures, we plot the MSE tendency term (in contours) to aid in interpretation. At a time lag of 10 days (about 25 days before the ISO peak over Indian/BoB longitudes, see Fig. 8a), it shows pronounced low-level (below 700 hPa) MSE build-up or increase in MSE tendency over 10°N, with similar signature in horizontal MSE advection. Corresponding distributions (figures not shown) of the moisture and temperature anomalies suggests that lower (upper) tropospheric MSE anomalies are almost entirely regulated by anomalous moisture (temperature). The low-level moistening continues to grow further and by day −5, it is moving toward the region at about 10°–15°N. Horizontal advection moistens the lower atmosphere north of 10°N, which opposes the decrease in tendency due to vertical advection (Fig. 9b). During the same period, the vertical advection is positive in the upper troposphere; partially coinciding with the positive anomalies in MSE tendencies (see Fig. 8b). The moistening of the lower atmosphere over the India/BoB region contributes to the destabilization of the atmosphere, as shown by an increase of CAPE values (see lower panel of Fig. 9b, c) at about 10°N–15°N. The dominance of horizontal advection in the low-level moistening (positive values of MSE tendency) over the

India/BoB region, compared to its vertical counterpart, brings the former to the fore as a driver in the chain of moist processes leading to ISO evolution. The origin of moistening over India and adjoining seas will be discussed in Sect. 5.

At day 0 (approximately 15 days before the ISO peak, Fig. 8c), moistening (positive anomaly in MSE tendency) occurs throughout the troposphere over the entire region (10°N–25°N) north of the equatorial deep convection (see Fig. 8c). This pronounced tropospheric moistening continues to prevail in day 5 as well (see Fig. 8d). Horizontal MSE advection mainly moistens the lower atmosphere over the India/BoB region (see Fig. 8c, d), and vertical MSE advection moistens throughout the troposphere above 500 hPa (see Fig. 9c, d). Here also, in the lower levels of the atmosphere, vertical advection still opposes the tendency due to horizontal advection. Over the tropical IO, the atmosphere begins to dry (see Fig. 8c, d), as indicated by negative anomalies in horizontal advection and tendency.

At day 10, the rainfall peak moves onto the India/BoB region at approximately 10°N–15°N and strong atmospheric moistening still occurs north to the region of large

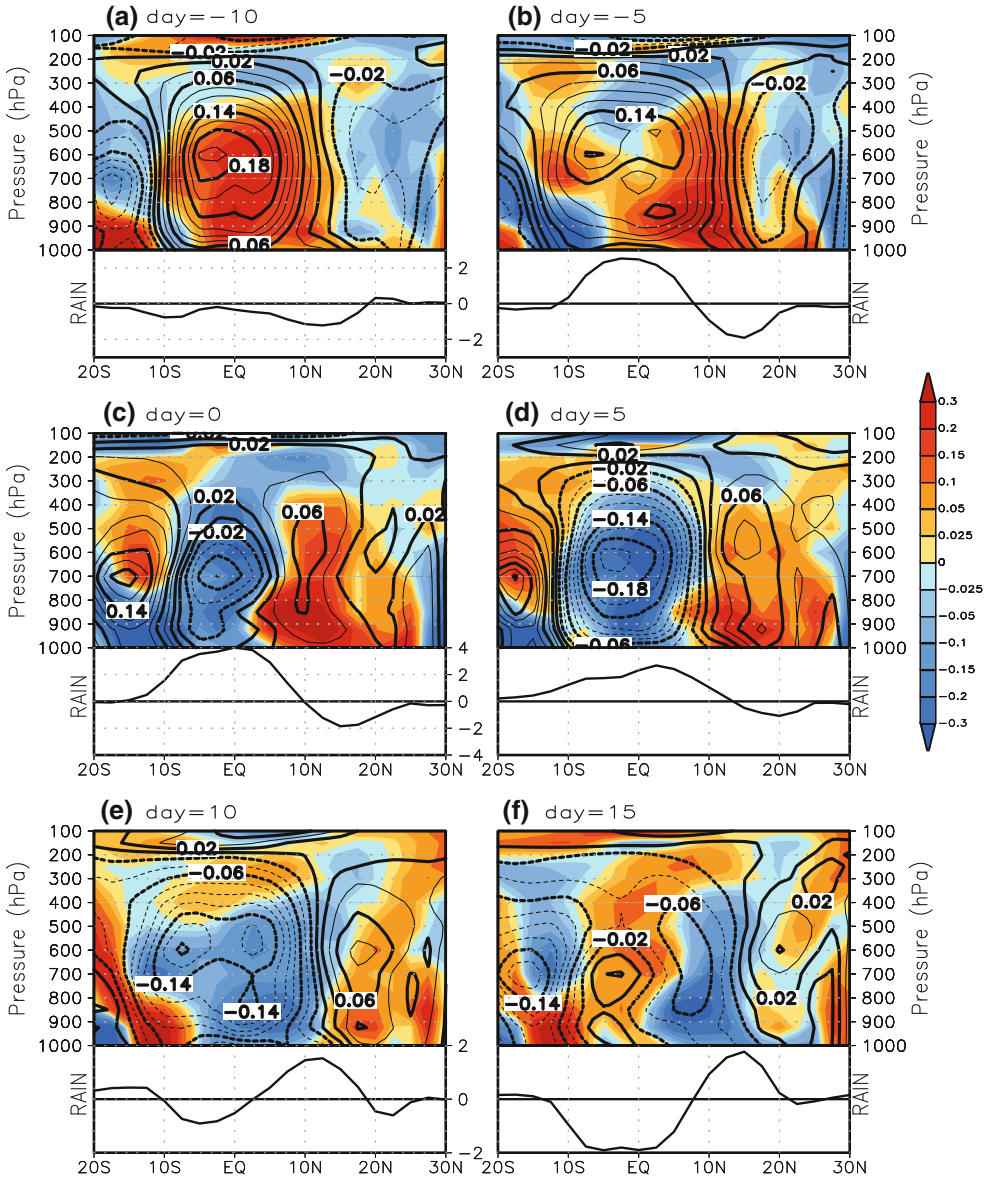

Fig. 8 Latitude-height maps of regressed anomalies (from CTRL simulation), showing the ISO evolution (lead/lag) of horizontal advection and tendency terms ($\times 10^{-2}$ J kg^{-1} s^{-1} units), averaged over 70°E–100°E. The corresponding evolution in rainfall anomalies (regressed, mm day^{-1}) are shown below in each *panel*. The contours denote the MSE tendency term and the shading represents the horizontal advection of MSE. First solid (*dashed*) contour is 0.02×10^{-2} (-0.02×10^{-2}) and the contour interval is 0.02×10^{-2} (-0.02×10^{-2}) J kg^{-1} s^{-1}. Regression is with respect to the base time series of rainfall averaged over EIO region

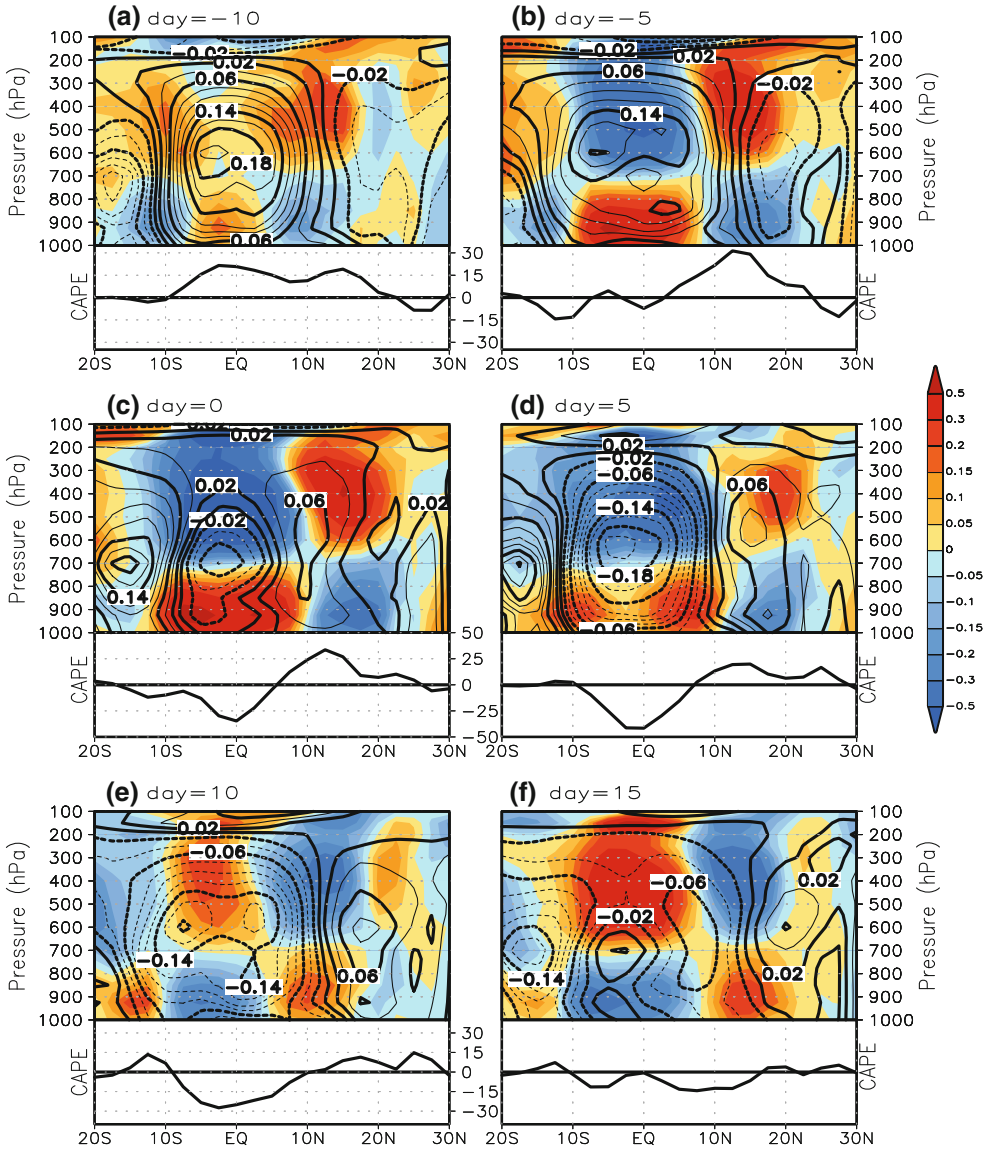

Fig. 9 Latitude-height maps of regressed anomalies (from CTRL simulation), showing the ISO evolution (lead/lag) of vertical advection and tendency terms ($\times 10^{-2}$ J kg^{-1} s^{-1} units), averaged over 70°E–100°E. The corresponding evolution in CAPE anomalies (regressed, J kg^{-1}) are shown below in each *panel*. The contours denote the MSE tendency and the shading represents the vertical advection of MSE. First solid (*dashed*) contour is 0.02×10^{-2} (-0.02×10^{-2}) and the contour interval is 0.02×10^{-2} (-0.02×10^{-2}) J kg^{-1} s^{-1}. Regression is with respect to the base time series of rainfall averaged over EIO region

precipitation. Horizontal advection continues to moisten the atmosphere north of 10°N (Fig. 8e). Coinciding with this rain peak, positive values of vertical advection tendencies appear below 700 hPa, indicating that MSE starts increasing from lower to higher levels over this region (Fig. 9e). At the same time, upper level moistening (by vertical advection) starts decreasing in intensity. The appearance of negative anomalies above 700 hPa is a manifestation of this. As the rainfall peak slowly progresses onto the region at approximately 15°N–20°N (from day 10 to day 15), this lower level moistening due to vertical advection anomalies grows in strength and size, extending into all Indian/BoB latitudes. At day 15, when the precipitation anomalies reach their maxima, the tendency anomalies over the India/BoB region are positive in the upper troposphere but negative in the lower troposphere, consistent with the general understanding on convection stabilizing the atmosphere (Fig. 8f). At the same time, precipitation reaches minima over the tropical IO (Fig. 8f) and the lower troposphere begins to be moistened, which may indicate that the pre-conditioning moistening process is occurring over there for the next ISO cycle.

In brief, the injection of MSE or moisture (in the lower troposphere) to the Indian/BoB region starts approximately

20 days before the precipitation maximum there (see Fig. 8b). Horizontal advection continues to grow in both space and time, and the resultant moistening makes the lower atmosphere unstable (see the CAPE values in the lower panels of Fig. 9b–d), causing the poleward movement of convection. During enhanced convection, vertical velocity is negative in the lower levels with a mid-tropospheric maximum and MSE increases from low to mid levels, resulting in a positive gradient in the vertical advection of MSE. The evolution of the vertical advection of MSE over the equatorial IO (see Fig. 9b–c) and India/BoB region (see Fig. 9e–f) further supports this interpretation, with an increase of vertical advection from low to mid levels. This positive gradient from low to mid levels implies enhanced low-level instability. So, the enhanced instability at lower levels in conjunction with pronounced tropospheric moistening augments the vertical growth of clouds, with modest contribution from the radiative heating (see Fig. 7h). These moistening processes are observed from the reanalysis as well (figure not shown); however, the low level moistening is somewhat weaker compared to the model.

Previous results (e.g. Johnson et al. 1999; Kiladis et al. 2005; Tung et al. 1999) suggest that shallow cumulus clouds and associated vertical motions are important for moistening the lower troposphere before the onset of MJO convection, which could contribute to the vertical advection term of the MSE budget (1). Considering these aspects, and for understanding the importance of shallow cumulus clouds to the model ISO characteristics, we conducted a sensitivity analysis without shallow convection, as described in Sect. 6.

5 The origin of advection induced moistening

Here we examine the relative contributions from horizontal wind and the MSE gradient in order to better illustrate the origin of the aforementioned moistening process. We break down the advection anomalies into terms involving only horizontal wind anomalies or only anomalous MSE gradient, in order to highlight the contribution from the climatological and anomalous components. The anomalous horizontal MSE advection can be partitioned as follows:

$$\left(\overrightarrow{V}\cdot\nabla m\right)' = \overrightarrow{V^c}\cdot\nabla m' + \overrightarrow{V'}\cdot\nabla m^c + \overrightarrow{V'}\cdot\nabla m' + \overrightarrow{V''}\cdot\nabla m'' \quad (2)$$

where "c" denotes the climatology term and the prime stands for daily anomalies. The first term on the right-hand side of (2) represents the advection associated with the climatological wind component acting on the anomalous MSE gradient. The second term denotes the advection due to the anomalous wind acting on the climatological MSE gradient. The third term is the contribution from the advection associated with anomalous wind acting on the anomalous MSE gradient. The last term is the residual due to transient variability which is very small compared to the rest of the terms. The terms in Eq. (2) are band-pass filtered (20–90 days) before the lag-regression analysis, shown in Fig. 10. As we are interested in propagation into the India/BoB region, we restrict our subsequent discussions to this region.

Figure 10b–d show the lag-latitude distribution of the advection terms (in shaded contours) from (2). A comparison with Fig. 10a suggests that from day −5 to day 10, over the latitude region from 7°N to 15°N, the total MSE advection shows good correspondence with the term $\overrightarrow{V^c}\cdot\nabla m'$ (VclmMano, see Fig. 10b) and hence VclmMano dominates over the remainder, $\overrightarrow{V'}\cdot\nabla m^c$ (VanoMclm, see Fig. 10c) and $\overrightarrow{V'}\cdot\nabla m'$ (VanoMano, see Fig. 10d). The second component (VanoMclm) exhibits rather stationary features during this period, instead of the robust propagating characteristics shown in Fig. 10a, b. At the same time period, the third term (VanoMano, see Fig. 10d) shows comparatively smaller values over these latitudes. The contribution from the term VclmMano can be interpreted as follows. The summer mean cross-equatorial flow covers the entire equatorial IO, with a prevailing southwesterly boundary layer component over the northern IO region (figure not shown). Further, Fig. 5b-c shows a north–south gradient in precipitation anomalies over the IO region (60°E–100°E), with a similar signature in the tropospheric moisture (Fig. 6b). This pronounced north–south gradient, in conjunction with the climatological summer flow, results in the dominance of the term VclmMano (Fig. 10b), as the advection effect by the summer mean flow in the boundary layer further shifts the specific humidity center to the north of the convection, leading to the poleward movement of the convection.

The aforementioned process is a manifestation of the moisture–convection feedback mechanism operating on the simulated ISOs. Jiang et al. (2004) also speculated the same (role of moisture advection), but for the independent poleward moving ISO disturbances in ECHAM4 model integration, forced with climatological SST. According to them, the horizontal moisture advection northward of deep convection is caused by both the advection of anomalous moisture by the mean southerly flow in the planetary boundary layer and the advection of background moisture by the anomalous winds. The former one coincides with our interpretations regarding the contribution of climatological wind acting on the anomalous moisture gradient.

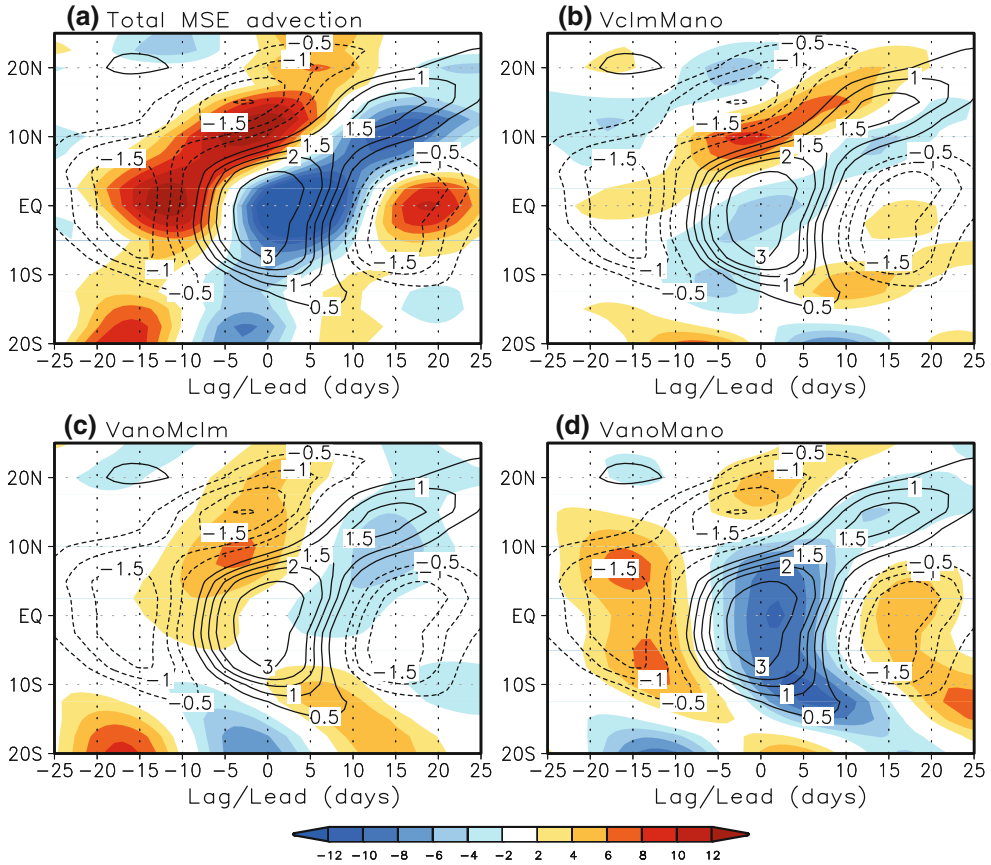

Fig. 10 **a** Lag-latitude diagrams of regressed rainfall (*contours*, mm day^{-1}) and MSE advection terms (*shaded*, W m^{-2}) averaged over 70°E–100°E, from CTRL simulation. **a** Total MSE advection, **b** climatological winds acting on anomalous MSE gradient (VclmMano), **c** anomalous winds acting on climatological MSE gradient (VanoMclm) and **d** anomalous winds acting on anomalous MSE gradient (VanoMano). All the budget terms shown here are vertically integrated estimates (from the surface to 100 hPa). Regression is with respect to the base time series of rainfall averaged over EIO region

However, in the model, there is relatively less contribution from the latter: anomalous wind acting on the climatological MSE gradient (VanoMclm, Fig. 10c).

6 Sensitivity tests

This section further evaluates the important components of the model (CFS with the RAS scheme) physics that are most effective for improving the BSISO simulation. In particular, the sensitivity of the ISO simulations (1) to shallow convection (EXP1) and (2) to convective rain evaporation and downdrafts (EXP2) is assessed. We hypothesize that the model performance on an intraseasonal time scale is sensitive to both the aforementioned changes in the parameterization. However, we note that every convective scheme interacts with its environment differently. Thus, implementing these parameterization changes into a different convective parameterization may not produce the same behavior. Note that in this study, only these elements are selected for evaluation because of the importance of these components on the moistening process associated with the ISO evolution, as described in the introduction. However, other processes such as microphysics, cloud–radiation interactions, and air–sea coupling are apparently important, but further studies are needed to precisely evaluate the impacts of them. As described in Sect. 2, coupled simulations conducted at the standard model resolution are used here for diagnostics.

6.1 ISO characteristics in sensitivity tests

Figure 11a, b show the wavenumber-frequency spectra for EXP1 and EXP2, respectively. EXP1 (Fig. 11a) shows a considerably reduced eastward propagating component with much less power than in the observation and CTRL (see Fig. 3a, b). Moreover, it fails to produce the corresponding spectral peak seen in the observation and model (see Fig. 3a, b), with much less variance on the intraseasonal time scale. Instead, the spectral peak is at a lower frequency (between 80 and 200 days) with a center at around 100 days (between wavenumbers 2 and 3). EXP2

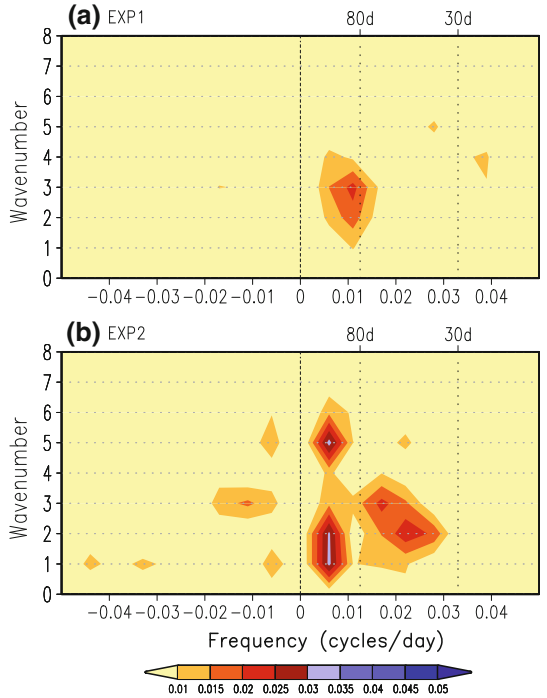

Fig. 11 Wavenumber-frequency spectra of equatorial (over EIO region) rainfall during the boreal summer season of **a** EXP1 and **b** EXP2. Individual May to October spectra were calculated for each year, and then averaged over all years of data. Only the climatological seasonal cycle was removed before calculation of the spectra. The units for spectrum are $mm^2\ day^{-2}$ per frequency interval per wave number interval. The bandwidth is $(180\ days)^{-1}$

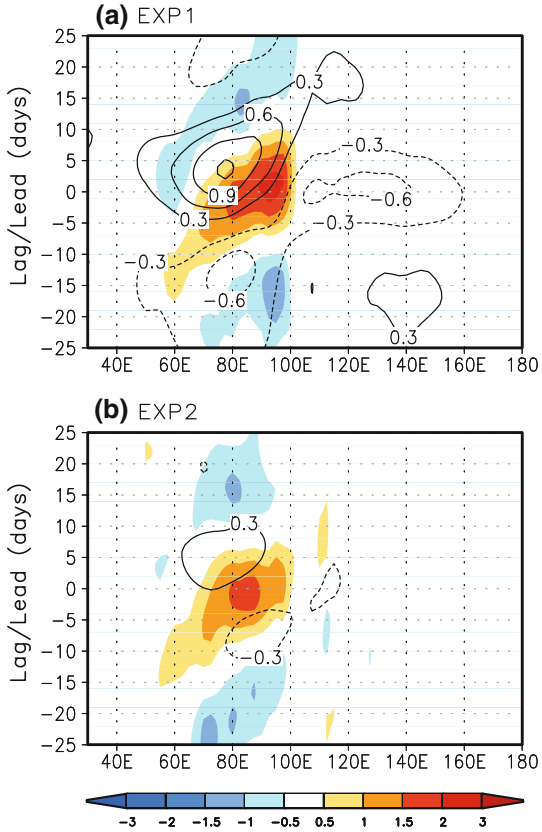

Fig. 12 Lag-longitude diagrams of regressed rainfall (mm day^{-1}, *shaded*) and 850 hPa zonal wind anomalies (m s^{-1}, *contours*), along the equator from **a** EXP1 and **b** EXP2. Regression is with respect to the base time series of rainfall averaged over EIO region

(Fig. 11b) also shows a remarkably reduced variance on the ISO time scale compared to the observations and CTRL. Furthermore, it shows multiple spectral peaks at lower frequencies (one between wavenumbers 1 and 3 and another between wavenumbers 4 and 6), with a period ranging between 100 and 200 days. Thus, these two experiments show a reduced magnitude of the power spectra in the intraseasonal band, suggesting that both components (shallow convection, and convective rain evaporation and downdrafts) are vital to the ISO characteristics. Further, both EXP1 and EXP2, with weaker anomalies (both in convection and circulation), fail to capture the eastward equatorial propagating disturbance from the IO to the western Pacific (see Fig. 12a, b), quite consistent with the results from the power spectrum. The zonal structure of the anomalies changed significantly in both experiments compared to CTRL (Fig. 2b). In particular, EXP2 (Fig. 12b) shows the weakest zonal wind signal, with no significant low-level convergence flow to the east of precipitation.

We next look at the poleward propagation characteristics in the sensitivity simulations, as shown in Fig. 13. Similar to the eastward propagating cases, the amplitudes of the poleward propagating disturbances are weakest in EXP2 (Fig. 13b). In addition, the meridional structure of the anomalies is totally disrupted with no discernable meridional propagating disturbances in zonal wind. EXP1 (Fig. 13a) seems to better capture the poleward propagating structure in rainfall and circulation anomalies, but shows weaker signals compared to those of observation and CTRL (Fig. 4a, b). These results indicate that, with the aforementioned changes in convective parameterization (shallow convection, and convective rain evaporation and downdrafts), the model is unable to sustain the large-scale convection–circulation coupling necessary for maintaining the ISO disturbance, irrespective of the atmospheric basic states.

In order to further discuss the importance of these components, we examine the vertical structure of intraseasonal MSE anomalies over the EIO as a function of time relative to peak precipitation anomalies. Vertical snapshots of the regressed anomalies are shown in Fig. 14 (regressed against the base point over the EIO) for the sensitivity simulations. The anomalous distribution from the CTRL (RAS simulation) is also shown for comparison (see Fig. 14a). As pointed out earlier, moisture dominates the

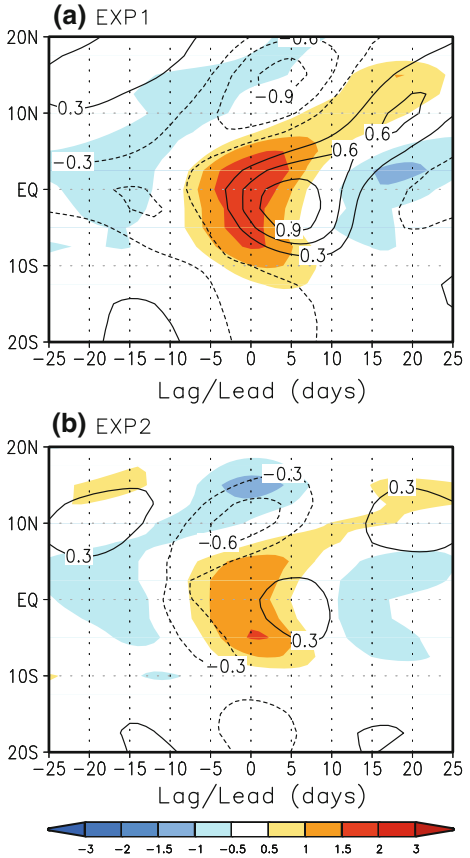

Fig. 13 Lag-latitude diagrams of regressed anomalies of rainfall (mm day^{-1}, *shaded*) and 850 hPa zonal wind (m s^{-1}, *contours*), averaged over 70°E–100°E from **a** EXP1 and **b** EXP2. Regression is with respect to the base time series of rainfall averaged over EIO region

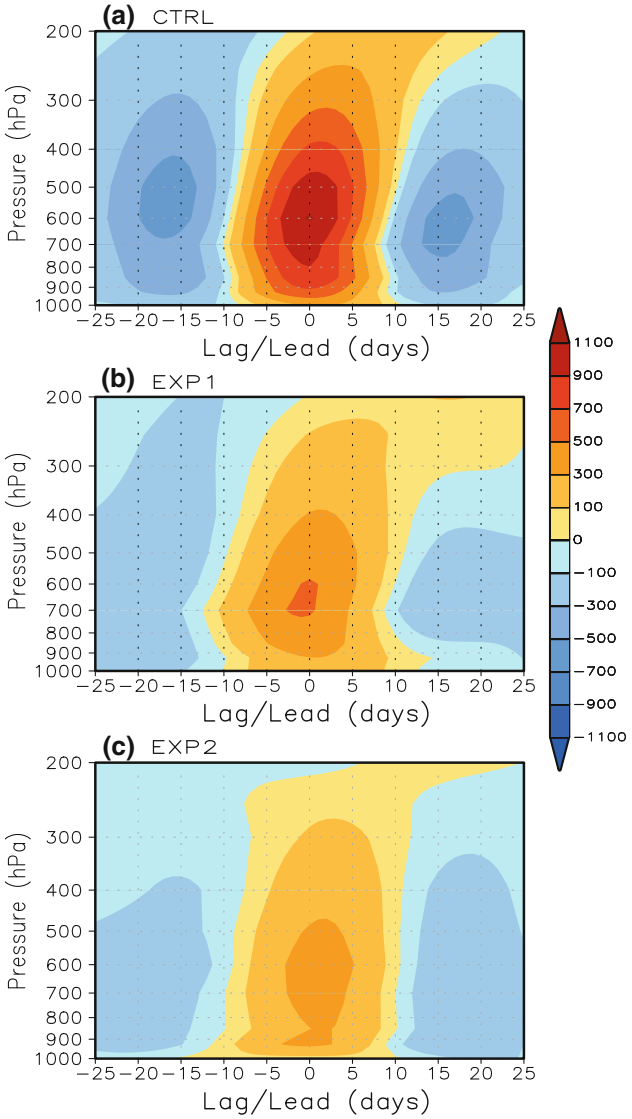

Fig. 14 Lag-height maps of regressed MSE anomalies (J kg^{-1}) over equatorial IO (EIO) for **a** CTRL, **b** EXP1 and **c** EXP2. Regression is with respect to the base time series of rainfall averaged over EIO region

MSE anomalies in the lower troposphere (below 400 hPa), while temperature regulates the upper tropospheric MSE anomalies. The lower tropospheric MSE anomalies in the CTRL show a steady increase from negative to positive values, indicating moistening process before the onset of intraseasonal convection, which is quite consistent with the observed features noted in earlier studies (e.g. Kemball-Cook and Weare 2001). The MSE anomalies in the middle troposphere peak at the point of maximum precipitation. After the passage of the rainfall peak, the sign of the MSE is reversed, indicating sharp dryness there. When the shallow convection is turned off (EXP1, Fig. 14b), the model completely fails to depict this pronounced MSE structure. In EXP2, the resultant positive anomalies in the lower to middle troposphere are considerably weaker (Fig. 14c).

It is interesting to note here that the peak lower tropospheric MSE anomalies in the model (CTRL simulation, see Fig. 14a) reach values within 700–900 J kg^{-1} at the point of maximum rainfall, quite consistent with other observational estimates (e.g. Kemball-Cook and Weare 2001). Since the model precipitation magnitude is also close to the observed values (see Fig. 4a, b), the convective parameterization (RAS) in the CFS model seems to produce the same build-up of instability as in the observations.

The effect of shallow cumulus and congestus is to moisten the lower (and middle) troposphere ahead of deep convection, as shown in observational studies (e.g. Khouider and Majda 2006; Kiladis et al. 2005). Shallow convection and the associated shallow heating and vertical motion profiles would be accompanied by convergence near the cloud base and divergence near the cloud top level. The CTRL simulation consistently indicates substantial lower tropospheric moistening prior to the intraseasonal convective peak. The weak MSE anomalies in EXP1 point

out that the abovementioned features are not well represented in it, indicating the missing cloud physics in EXP1 (Fig. 14b). Additional examination of vertical distributions of anomalous vertical velocity and diabatic heating from EXP1 shows considerably reduced amplitude (figures not shown), further supporting the robust role of shallow convection on the model ISO characteristics.

Downdrafts and rain evaporation considerably moisten the lower and middle troposphere in the mean (see Subsect. 6.2). In the case of downdrafts, Johnson (1976) previously carried out a diagnostic model study (using a one dimensional entraining plume model to represent cumulus updrafts and downdrafts) for understanding the effect of convective scale updrafts and downdrafts on the thermodynamic properties of large-scale atmospheric circulation. They found that convective downdrafts can lead to weaker compensating subsidence away from convection. Therefore, downdraft promotes a moister lower and middle troposphere, in addition to the direct moistening effects by rainfall evaporation. In agreement with this, the CTRL simulation clearly shows pronounced moistening due to rain evaporation in the middle troposphere. The vertical distributions in EXP2 (see Fig. 14c) demonstrate less water vapor content in the lower to mid levels, a clear manifestation of the absence of convective evaporation and downdrafts.

All the aforementioned diagnostics highlight the importance of the processes of interest here (shallow convection and convective rain evaporation and downdrafts). These processes play critical roles in the development and propagation characteristics of ISOs and have a significant involvement in the large-scale organization of tropical convective cloudiness, as seen in the observations.

6.2 Relative humidity (RH)–precipitation relationship

In this section, the structures of relative humidity (RH) and precipitation rate and their fundamental physical relationship are assessed for a more detailed understanding of ISO related precipitation variation. This diagnostic is inspired by a previous observational study (Bretherton et al. 2004) that showed the importance of this metric (RH–precipitation relationship). Such diagnostic assessments are needed as global climate models often produce an excessively dry environment and overly frequent light rainy days that prevent complete organization of the equatorial convective system (Thayer-Calder and Randall 2009; Xavier 2012). Further, simplified models have also demonstrated the significance of this metric in determining the time and space scale of the ISO (Raymond 2001).

Composite vertical profiles of RH categorized by daily average rainfall over the ASM region (30°E–120°E, 30°S–30°N) are shown in Fig. 15. The corresponding

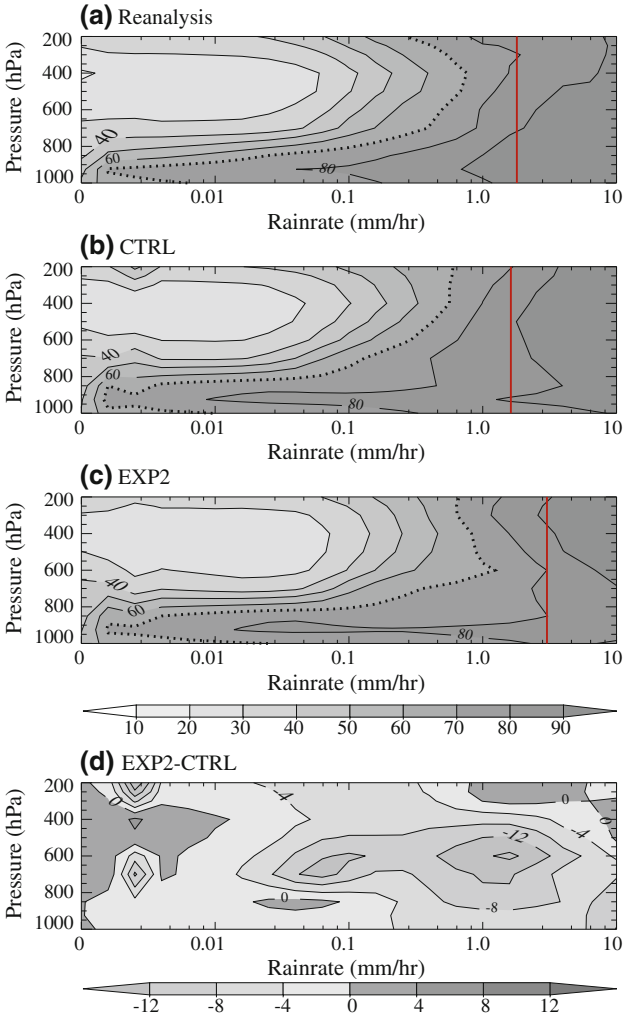

Fig. 15 Composite vertical cross section of relative humidity (with contour intervals of 10 %) categorized by daily average rainfall (mm h^{-1}) over the summer Asian monsoon region (30°E–120°E, 30°S–30°N) for **a** reanalysis, **b** CTRL, **c** EXP2, and **d** difference (EXP2–CTRL). In **a**, **b** and **c** the 70 % contour is *dotted* for clarity in presentation. The *vertical red line* represents the rain rate at which the entire tropospheric column becomes nearly saturated

profile from the reanalysis is also shown for comparison (Fig. 15a). In both the reanalysis and CTRL (see Fig. 15a, b), the RH in the lower troposphere gradually increases with rain rate. For intensities above 0.6 mm h^{-1} (approximately 15 mm day^{-1}), the entire troposphere becomes rather uniformly humid or moistened, as indicated by the 70 % contour (shown in dotted contours). Again, in both the reanalysis and CTRL, the entire column is nearly fully saturated (indicated by a red line) for a rain rate above 1.6 mm h^{-1} (about 40 mm day^{-1}), suggesting the interpretation that heavy precipitation coincides with a nearly saturated column. EXP2 (Fig. 15c), however, attains a nearly uniform moist column at higher rain rate thresholds (above 24 mm day^{-1}), showing an unrealistic lack of moistening and therefore a dry bias in the lower levels to

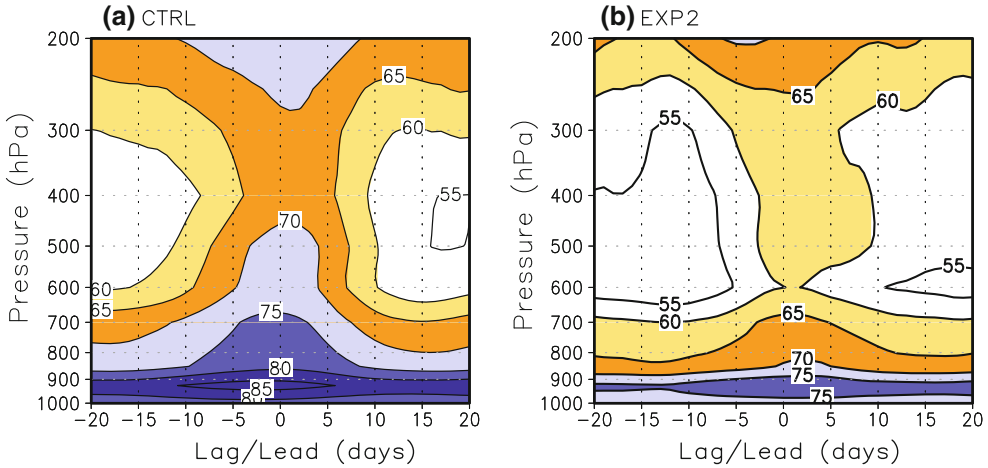

Fig. 16 Composite vertical profile of relative humidity for strong rainfall events over the equatorial IO region (EIO), from **a** CTRL and **b** EXP2. *Contour lines* are in 5 % increments. The composite is formed for the cases where the normalized rainfall index over the EIO region, exceeds 1 standard deviation

500 hPa (see Fig. 15d). In particular, it shows two centers of pronounced dry bias (between 700 and 500 hPa levels), one centered at a rain rate of about 1 mm h^{-1} and another centered at a mid intensity rate of 0.04 mm h^{-1}. Accordingly, the very moist columns for middle to higher rain rates are not realistic in EXP2, in contrast to the pronounced distributions in reanalysis and CTRL (see Fig. 15a, b). Furthermore, in EXP2 (Fig. 15c), the entire column is nearly completely saturated only at heavy rain intensity above 2.5 mm h^{-1} (approximately 60 mm day^{-1}), and hence, the heavy rainfall is suppressed until a high precipitation threshold is reached.

To further clarify the effect of EXP2 on model ISO, we now present the lead/lag composite profiles of RH for the selected strong rainfall events in Fig. 16. The strong events are selected over the EIO region using a rainfall threshold of 1 standard deviation (that is, the composite is made for the cases where the normalized rainfall index over the EIO region, exceeds 1 standard deviation). CTRL (Fig. 16a) shows an increase in RH through the boundary layer to the mid troposphere before the passage of the ISO over the equatorial IO. A rapid reduction in moisture follows, especially in the free troposphere, after the passage of the rainfall peak. EXP2 (Fig. 16b), on the other hand, fails to buildup a thick humid layer. At the point of heaviest convection at day 0, there is some indication of an increase below the boundary layer, but in general, the column is much drier and the boundary layer is not as thick as seen during the passage of the ISO in CTRL. All these findings indicate that downdrafts and rain evaporation promote a moister mean tropical troposphere and increase in tropical rainfall. Hence, our results here show that the artificial suppression of the downdraft and rain evaporation process in the deep convective parameterization leave a signature throughout the tropical atmosphere.

Regarding the effect of shallow convection on precipitation, recently Seo et al. (2012), using the same model configurations (CFS model with RAS scheme), observed that the removal of shallow convection produced more frequent drizzle and light rain rates (0–0.1 mm h^{-1}) compared to their control simulation (see Fig. 10 of Seo et al. 2012). According to them, for drizzle or light rain rates, it showed a more humid environmental air in the boundary layer (below 850 hPa). Subsequently, they hypothesized that drizzle and light rain tend to cool the boundary layer, stabilizing it. Thus instability is reduced which consequently leads to less intense convection.

7 Summary and concluding remarks

The NCEP Climate Forecast System (CFS) with the RAS convection scheme of Moorthi and Suarez (1999) exhibits better performance in representing boreal summer intraseasonal variability over the tropical Indo-Pacific region, as compared with simulation using the SAS convection scheme. The standard CFS with SAS produces intraseasonal variability (eastward component along equator) in both zonal winds and precipitation that is much lower than is observed. Its northward component is also weak with little variability in precipitation and zonal winds. The RAS scheme (CTRL simulation) produces realistic intraseasonal variability in both wind and precipitation, capturing both eastward and northward propagating characteristics. The convection is initiated over the central IO, similar to observations, and enhanced and suppressed convection

anomalies exhibit the observed multiple regional heat sources. The steady, continuous poleward propagation of the rainfall anomaly over the IO is also well captured. The model (CTRL simulation) differs from the observed intraseasonal features as follows: error in the eastward extension of equatorial convection into the central equatorial Pacific, biases in the spatial structure of precipitation anomalies over the Indian subcontinent, and strong ISO variability as evident in the frequency-wave spectrum of model precipitation.

The first part of our study examines the intraseasonal MSE budget to elucidate the relevant moist and thermodynamic processes, associated with BSISO in the CFS model. By analyzing the column integral, it provides specific details on how moist convection in the model redistributes MSE. Moreover, the budget analysis offers a useful framework to assess the importance of various processes, as revealed from the examination of the individual terms of the budget. We map the spatial distributions (both vertical and horizontal) of the budget components contributed from the changes in large-scale circulation for different phases of the monsoon ISO (relative to time when precipitation over the equatorial IO reaches maximum). This demonstrates the interaction between moist physics and circulation.

Our model budget results show a coherent, correct phase relationship between precipitation and moist and thermodynamic variables for northward propagation. Horizontal advection and surface turbulent heat fluxes are dominant components for the propagation tendencies of the budget, where latent heating is dominated by the wind-driven component. Furthermore, in the model, surface enthalpy fluxes, consisting of radiative and surface turbulent heat flux components, contribute to the maintenance of the ISO anomalies. This source of energy is balanced by sinks due to the advection components of MSE. These inferences appear to be consistent with our diagnostics using ERA and other similar investigations using reanalysis data sets and models (e.g. Maloney 2009; Boos and Kuang 2010; Kiranmayi and Maloney 2011). However, compared to these studies, our present results show that the model derived MSE estimate has a comparatively smaller contribution from the net radiative fluxes (mainly longwave estimates) for the propagation tendencies. Over the India/BoB region (at lead 0), the longwave estimates in the model are approximately one-half of the amplitude observed in reanalysis outputs, imposing an equivalent reduction on the model net radiative flux.

From the model budget analysis, the following inferences can be drawn. Over the Indian/BoB region, the injection of MSE or moisture (in the lower troposphere) starts (see Fig. 8b) approximately 20 days before the precipitation maximum there. Horizontal advection continues to grow in both space and time, and the resultant moistening destabilizes the atmosphere (see CAPE values in the lower panels of Fig. 9), causing the poleward movement of convection. The climatological wind acting on the anomalous moisture gradient mainly contributes to the moistening process over the India/BoB region, as confirmed by examination of the moisture advection equation (see Sect. 5). This process is in agreement with the moisture–convection feedback mechanism (e.g. Jiang et al. 2004). Surface enthalpy flux anomalies oppose the propagation tendencies formed by horizontal advection, with the surface turbulent heat fluxes dominating. The implication is that in the model, wind–evaporation feedback dominates over cloud–radiation feedback for poleward ISO propagation. Wind–evaporation feedback causes the propagation characteristics as well as the recharge/discharge process to be more gradual than if horizontal advection were acting alone. This interplay between surface flux tendencies and advection tendencies may have consequences for the time scale of ISO variability in the model. In short, the intraseasonal budget diagnostics performed here illustrate how the regulation by column MSE dominates the tropical ISO. Further, the interaction between moist physics and regional circulation and the role of wind–evaporation and cloud–radiation feedbacks are crucial to the dynamics of tropical ISO variability.

The second part of our work is based on sensitivity studies using the CFS model with the RAS parameterization scheme. The important components of the model physics responsible for the realistic simulation of intraseasonal characteristics are examined, particularly focusing upon the moistening processes. The experiments are designed such that certain components in the model convection scheme are not allowed. Accordingly, we have two sets of experiments, one turning off the component related to shallow convection (EXP1) and the other switching off the related subroutines of the convective precipitation evaporation and downdraft process (EXP2). The sensitivity tests (Sect. 6) suggest that both the shallow convection and the convective precipitation evaporation and downdrafts are crucial to the success of the RAS scheme in simulating ISO characteristics. Removal of these components greatly reduces the amplitude of the BSISO in the CFS. The wavenumber-frequency power spectrum analysis shows that both EXP1 and EXP2 are unable to simulate the spectral peaks in the intraseasonal band, for the eastward propagating component of the BSISO (see Fig. 11a, b). Consistently, both experiments failed to capture both eastward and northward propagating disturbances (in both precipitation and circulation, see Figs. 12a, b, 13a, b). The associated vertical structures of moist and thermodynamic variables are also weaker compared to CTRL (see Fig. 14a, c), suggesting the fundamental importance of moist and

thermodynamic preconditioning processes on the ISO characteristics. The results also indicate that in the absence of these components, the model is unable to keep up the large-scale convection–circulation feedback necessary for maintaining the ISO disturbance.

Successful simulation of the complex space–time evolution of the BSISO, capturing both the propagating modes, is still in the early stages of development and seems to be a difficult venture for all global models. Nevertheless, some members of the current generation of models show substantial improvement over earlier versions, and efforts are still underway to achieve significant improvements. The results of our study suggest the following elements and details that a model must account for in order to correctly simulate the ISO. As per our results, horizontal MSE advection appears to have a significant effect on the ISO mode. Therefore, first, the interaction between moist physics and convection and the consequent feedback from large-scale circulation needs to be faithfully represented in dynamical models. Furthermore, the importance of the specific humidity gradient in our results warrants that the regional variation of moisture flow ought to be included.

The second recommendation derived from our results is the true representation of surface enthalpy fluxes, dominantly consisting of surface latent heat and longwave radiation fluxes, in the models. Hence, both must be of sufficiently large magnitude to regulate the effects of horizontal advection on the MSE recharge-discharge process. Otherwise, if horizontal advection were acting alone, it would have significant implications for the propagation characteristics: an increase in propagation speed and a shorter propagation time scale. In this regard, recently Boos and Kuang (2010), using sensitivity tests, suggested that wind–evaporation feedback significantly slows down the poleward propagation of anomalies. The importance of radiation flux as noted from the budget estimates of reanalysis indicates the significant role of cloud–radiation feedback on ISO propagation, which is in contrast to the model (CTRL simulation) MSE estimates. Even though the role of radiative fluxes needs consensus from other reanalysis data sets, to some extent, this emphasizes the significance of the parameterization of cloud–radiation interaction, which needs to be faithfully represented in models.

The last recommendation comes from our sensitivity studies, which suggest problems in the representation of the RH–precipitation relationship and the preconditioning (moist and thermodynamic) ahead of the ISO. The fundamental physical relationship between moisture and precipitation is highly relevant, and hence, the representation of it in models is vital to simulate the realistic ISO. However, seamless improvement is subjected to constraints due to the complex feedbacks involved. Recent diagnostic studies further support our findings. Xavier (2012) showed that most of the Coupled Model Intercomparison Project 3 (CMIP3) models have biases in representing rainfall characteristics in general and ISO in particular. Some of these biases are shown to be related to the problems cited above: a deficiency in the representation of the RH-precipitation relationship and the moisture preconditioning process. Moreover, a study by John and Soden (2007) also show that most CMIP3 models have a mean dry bias in the boundary layer. Xavier (2012) partly attributes this bias to the uncertainties in representing shallow cumulus, convective downdrafts, and convective detrainment, and they suggest the need for improved representation of these processes for the successful simulation of the ISO. In the light of the above, our results assume scientific significance and the insights gained here would be highly beneficial to the convection parameterization community.

Our results suggest that ISO simulation in the CFS with the RAS scheme is sensitive to the parameterization of both the shallow convection (EXP1) and the convective rain evaporation and downdrafts (EXP2). However, we do not know whether the present results are model dependent. Hence, we wish to note here that the present study does not argue that implementing RAS parameterization of downdrafts and rain evaporation in other convection schemes will essentially improve intraseasonal variability, as each convective scheme interacts with its environment differently. Thus, similar sensitivity experiments need to be conducted with other coupled models to test the robustness of our results. As one last note, our model budget estimates and subsequent inferences are only compared against the ERA. Therefore, the present model results need to be verified with other reanalysis products and models, for consistency.

Acknowledgments The first author sincerely thanks Mr. Jinho Choi for all the support in performing the sensitivity experiments. This work is supported by the Korea Meteorological Administration Research and Development Program under Grant CATER 2012–3071 and by the National Research Foundation of Korea (NRF) Grant funded by the Korea government (MEST) (No. 2011-0015486). We also thank the anonymous reviewers for their constructive comments. The authors acknowledge the support of the Korea Institute of Science and Technology Information (KISTI).

References

Ajayamohan RS, Goswami BN (2007) Dependence of simulation of boreal summer tropical intraseasonal oscillations on the simulation of seasonal mean. J Atmos Sci 64:460–478

Ajayamohan RS, Annamalai H, Luo JJ, Hafner J, Yamagata T (2010) Poleward propagation of boreal summer intraseasonal oscillations in a coupled model: role of internal process. Clim Dyn 37:851–867

Andersen JA, Kuang Z (2012) Moist static energy budget of MJO-like disturbances in the atmosphere of a zonally symmetric aquaplanet. J Clim 25:2782–2804

Annamalai H, Slingo JM (2001) Active/break cycles: diagnosis of the intraseasonal variability of the Asian summer monsoon. Clim Dyn 18:85–102

Arakawa A, Schubert WH (1974) Interaction of cumulus cloud ensemble with the large-scale environment. Part I. J Atmos Sci 31:674–701

Back LE, Bretherton CS (2006) Geographic variability in the export of moist static energy and vertical motion profiles in the tropical Pacific. Geophys Res Lett 33:L17810. doi:10.1029/2006GL026672

Benedict JJ, Randall DA (2007) Observed characteristics of the MJO relative to maximum rainfall. J Atmos Sci 64:2332–2354

Berrisford P, Dee D, Fielding K, Fuentes M, Kallberg P, Kobayashi S, Uppala S (2009) The ERA-interim archive. ERA report series 1, 16 pp

Bhat GS, Vecchi GA, Gadgil S (2004) Sea surface temperature of the Bay of Bengal derived from the TRMM microwave imager. J Atmos Ocean Technol 21:1283–1290

Boos WR, Kuang Z (2010) Mechanisms of poleward propagating, intraseasonal convective anomalies in cloud system-resolving models. J Atmos Sci 67:3673–3691

Boyle J, Klein S, Zhang G, Xie S, Wei X (2008) Climate model forecast experiments for TOGA COARE. Mon Weather Rev 136:808–832

Bretherton CS, Peters ME, Back LE (2004) Relationships between water vapor path and precipitable water over the tropical oceans. J Clim 17:1517–1528

Byun YH, Hong SY (2004) Impact of boundary layer processes on simulated tropical rainfall. J Clim 17:4032–4044

Cheng MD (1989) Effects of downdrafts and mesoscale convective organizations on heat and moisture budget of tropical cloud clusters. Part II: effects of convective-scale downdrafts. J Atmos Sci 46:1517–1564

Chou C, Hsueh YC (2010) Mechanisms of northward-propagating intraseasonal oscillation—a comparison between the Indian Ocean and the Western North Pacific. J Clim 23:6624–6640

Duchon C (1979) Lanczos filtering in one and two dimensions. J Appl Meteorol 18:1016–1022

Emanuel KA (1987) An air-sea interaction model of intraseasonal oscillations in the tropics. J Atmos Sci 44:2324–2340

Fu X, Wang B (2009) Critical roles of the stratiform rainfall in sustaining the Madden–Julian oscillation: GCM experiments. J Clim 22:3939–3959

Fu X, Wang B, Li T, McCreary J (2003) Coupling between northward propagating intraseasonal oscillations and sea-surface temperature in the Indian Ocean. J Atmos Sci 60(15):1733–1753

Goswami BN (2005) South Asian monsoon. In: Lau WKM, Waliser DE (eds) Intraseasonal variability in the atmosphere-ocean climate system. Praxis Springer, Berlin, pp 19–61

Goswami BN, Shukla J (1984) Quasi-periodic oscillations in a symmetric general circulation model. J Atmos Sci 41:20–37

Hendon HH, Glick J (1997) Intraseasonal air-sea interaction in the tropical Indian and Pacific Oceans. J Clim 10:647–661

Holton JR (1982) An introduction to dynamic meteorology. Academic Press, Dublin

Huffman GJ, Adler RF, Morrissey M, Bolvin DT, Curtis S, Joyce R, McGavock B, Susskind J (2001) Global precipitation at one-degree daily resolution from multi-satellite observations. J Hydrometeor 2:36–50

Inness P, Slingo J (2003) Simulation of the Madden–Julian oscillation in a coupled general circulation model. Part I: comparison with observations and an atmosphere-only GCM. J Clim 16:345–364

Jiang X, Li T, Wang B (2004) Structures and mechanisms of the northward propagating boreal summer intraseasonal oscillation. J Clim 17:1022–1039

John VO, Soden BJ (2007) Temperature and humidity biases in global climate models and their impact on climate feedbacks. Geophys Res Lett 34:L18704. doi:10.1029/2007GL030429

Johnson RH (1976) Role of convective-scale precipitation downdrafts in cumulus and synoptic-scale interactions. J Atmos Sci 33:1890–1910

Johnson RH, Rickenbach TM, Rutledge SA, Ciesielski PE, Schubert WH (1999) Trimodal characteristics of tropical convection. J Clim 12:2397–2418

Kanamitsu M, Ebisuzaki W, Woollen J, Yang SK, Hnilo JJ, Fiorino M, Potter GL (2002) NCEP-DOE AMIP-II reanalysis (R-2). Bull Am Meteorol Soc 83:1631–1643

Kao CYJ, Ogura Y (1987) Response of cumulus clouds to large-scale forcing using the Arakawa–Schubert cumulus parameterization. J Atmos Sci 44:2437–2458

Kemball-Cook SR, Wang B (2001) Equatorial waves and air–sea interaction in the boreal summer intraseasonal oscillation. J Clim 14:2923–2942

Kemball-Cook SR, Weare BC (2001) The onset of convection in the Madden–Julian oscillation. J Clim 14:780–793

Kemball-Cook SR, Wang B, Fu X (2002) Simulation of the intraseasonal oscillation in the ECHAM-4 model: impact of coupling with an ocean model. J Atmos Sci 59:1433–1453

Khouider B, Majda AJ (2006) A simple multicloud parameterization for convectively coupled tropical waves. Part I: linear analysis. J Atmos Sci 63:1308–1323

Kikuchi K, Takayabu YN (2004) The development of organized convection associated with the MJO during TOGA COARE IOP: trimodal characteristics. Geophys Res Lett 31:L10101. doi:10.1029/2004GL019601

Kiladis GN, Straub KH, Haertel PT (2005) Zonal and vertical structure of the Madden–Julian oscillation. J Atmos Sci 62:2790–2809

Kiladis GN, Wheeler MC, Haertel PT, Straub KH, Roundy PE (2009) Convectively coupled equatorial waves. Rev Geophys 47:RG2003. doi:10.1029/2008RG000266

Kiranmayi L, Maloney ED (2011) Intraseasonal moist static energy budget in reanalysis data. J Geophys Res 116:D21117. doi:10.1029/2011JD016031

Krishnan R, Zhang C, Sugi M (2000) Dynamics of breaks in the Indian summer monsoon. J Atmos Sci 57:1354–1372

Lau KM, Chan PH (1986) Aspects of the 40–50 day oscillation during the northern summer as inferred from the outgoing longwave radiation. Mon Weather Rev 114:1354–1367

Lau KM, Peng L (1990) Origin of low-frequency (intraseasonal) oscillations in the tropical atmosphere. Part III: monsoon dynamics. J Atmos Sci 47:1443–1462

Lawrence DM, Webster PJ (2002) The boreal summer intraseasonal oscillation: relationship between northward and eastward movement of convection. J Atmos Sci 59:1593–1606

Lin JL, Mapes BE (2004) Radiation budget of the tropical intraseasonal oscillation. J Atmos Sci 61:2050–2062

Lin JL et al (2006) Tropical intraseasonal variability in 14 IPCC AR4 climate models. Part I: convective signals. J Clim 19:2665–2690

Lin JL, Weickman KM, Kiladis GN, Mapes BE, Schubert SD, Suarez MJ, Bacmeister JT, Lee MI (2008) Subseasonal variability associated with Asian summer monsoon simulated by 14 IPCC AR4 coupled GCMs. J Clim 21:4541–4567

Madden RA, Julian PR (1994) Observations of the 40–50-day tropical oscillation—a review. Mon Weather Rev 122:814–837

Maloney ED (2009) The moist static energy budget of a composite tropical intraseasonal oscillation in a climate model. J Clim 22:711–729

Maloney ED, Hartmann DL (2001) The sensitivity of intraseasonal variability in the NCAR CCM3 to changes in convective parameterization. J Clim 14:2015–2034
Maloney ED, Sobel AH (2004) Surface fluxes and ocean coupling in the tropical intraseasonal oscillation. J Clim 17:4368–4386
Moorthi S, Suarez MJ (1999) Documentation of version 2 of relaxed Arakawa–Schubert cumulus parameterization with convective downdrafts. NOAA Tech. Rep. NWS/NCEP 99-01, 44 pp
Moorthi S, Pan HL, Caplan P (2001) Changes to the 2001 NCEP operational MRF/AVN global analysis/forecast system. NWS Technical Procedures Bulletin 484, 14 pp
Neelin JD, Held IM (1987) Modeling tropical convergence based on the moist static energy budget. Mon Weather Rev 115:3–12
Pacanowski RC, Griffies SM (1998) MOM 3.0 manual. NOAA/Geophysical Fluid Dynamics Laboratory, Princeton, p 668
Pan HL, Wu WS (1995) Implementing a mass flux convective parameterization package for the NMC Medium-Range Forecast model. NMC Office Note 409, 40 pp
Peters ME, Bretherton CS (2006) Structure of tropical variability from a vertical mode perspective. Theor Comput Fluid Dyn 20:501–524
Raymond DJ (2000) The Hadley circulation as a radiative-convective instability. J Atmos Sci 57:1286–1297
Raymond DJ (2001) A new model of the Madden–Julian oscillation. J Atmos Sci 58:2807–2819
Raymond DJ, Fuchs Z (2009) Moisture modes and the Madden–Julian oscillation. J Clim 22:3031–3046
Saha S et al (2006) The NCEP climate forecast system. J Clim 19:3483–3517
Salby ML, Hendon HH (1994) Intraseasonal behavior of clouds, temperature, and motion in the tropics. J Atmos Sci 51:2207–2224
Sengupta D, Goswami BN, Senan R (2001) Coherent intraseasonal oscillations of ocean and atmosphere during the Asian summer monsoon. Geophys Res Lett 28:4127–4130
Seo KH, Wang W (2010) The Madden–Julian oscillation simulated in the NCEP climate forecast system model: the importance of stratiform heating. J Clim 23:4770–4793
Seo KH, Xue Y (2005) MJO-related oceanic Kelvin waves and the ENSO cycle: a study with the NCEP global ocean data assimilation system. Geophys Res Lett 32:L07712. doi:10.1029/2005GL022511
Seo KH, Schemm JKE, Jones C, Moorthi S (2005) Forecast skill of the tropical intraseasonal oscillation in the NCEP GFS dynamical extended range forecasts. Clim Dyn 25:265–284
Seo KH, Schemm JKE, Wang W, Kumar A (2007) The Boreal summer intraseasonal oscillation simulated in the NCEP climate forecast system: the effect of sea surface temperature. Mon Weather Rev 135:1807–1827
Seo KH, Choi JH, Han SD (2012) Factors for the simulation of convectively coupled Kelvin waves. J Clim 25:3495–3514
Sikka DR, Gadgil S (1980) On the maximum cloud zone and the ITCZ over Indian longitudes during the south west monsoon. Mon Weather Rev 108:1840–1853
Simmons AJ, Uppala SM, Dee DP, Kobayashi S (2007) ERA-Interim: new ECMWF reanalysis products from 1989 onwards. ECMWF Newsl 110:25–35
Slingo JM et al (1996) Intraseasonal oscillations in 15 atmospheric general circulation models: results from an AMIP diagnostic subproject. Clim Dyn 12:325–357
Sobel AH, Johan N, Lorenzo MP (2001) The weak temperature gradient approximation and balanced tropical moisture waves. J Atmos Sci 58:3650–3665
Sobel AH, Maloney ED, Bellon G, Frierson DM (2008) The role of surface fluxes in tropical intraseasonal oscillations. Nat Geosci. doi:10.1038/ngeo312
Sperber KR, Annamalai H (2008) Coupled model simulations of boreal summer intraseasonal (30–50 day) variability, part I: systematic errors and caution on use of metrics. Clim Dyn 31:345–372. doi:10.1007/s00382-008-0367-9
Sperber KR, Gualdi S, Legutke S, Gayler V (2005) The Madden–Julian oscillation in ECHAM4 coupled and uncoupled general circulation models. Clim Dyn 25:117–140
Straub KH, Haertel PT, Kiladis GN (2010) An analysis of convectively coupled Kelvin waves in 20 WCRP CMIP3 global coupled climate models. J Clim 23:3031–3056
Sugiyama M (2009a) The moisture mode in the quasi-equilibrium tropical circulation model. Part I: analysis based on the weak temperature gradient approximation. J Atmos Sci 66:1507–1523
Sugiyama M (2009b) The moisture mode in the quasi-equilibrium tropical circulation model. Part II: nonlinear behavior on an equatorial β plane. J Atmos Sci 66:1525–1542
Thayer-Calder K, Randall DA (2009) The role of convective moistening in the Madden–Julian oscillation. J Atmos Sci 66:3297–3312
Tiedtke M (1983) The sensitivity of the time-mean large-scale flow to cumulus convection in the ECMWF model. ECMWF Workshop on Convection in Large-Scale Numerical Models. Reading, England, pp 297–316
Trenberth KE, Stephaniak DP (2003) Seamless poleward atmospheric energy transports and implications for the Hadley circulation. J Clim 16:3706–3722
Tung WW, Lin C, Chen B, Yanai M, Arakawa A (1999) Basic modes of cumulus heating and drying observed during TOGA-COARE IOP. Geophys Res Lett 26:3117–3120
Vecchi GA, Harrison DE (2002) Monsoon breaks and subseasonal sea surface temperature variability in the Bay of Bengal. J Clim 15:1485–1493
Waliser DE (1996) Formation and limiting mechanisms for very high sea surface temperature: linking the dynamics and thermodynamics. J Clim 9:161–188
Wang B, Rui H (1990) Synoptic climatology of transient intraseasonal convective anomalies. Meteorol Atmos Phys 44:43–61
Wang W, Schlesinger ME (1999) The dependence on convective parameterization of the tropical intraseasonal oscillation simulated by the UIUC 11-layer atmospheric GCM. J Clim 12:1423–1457
Wang B, Xie X (1997) A model for the boreal summer intraseasonal oscillation. J Atmos Sci 54:72–86
Webster PJ (1983) Mechanism of monsoon low-frequency variability: surface hydrological effects. J Atmos Sci 40:2110–2124
Webster PJ, Yang S (1992) Monsoon and ENSO: selectively interactive systems. Q J Meteorol Soc 118:877–926
Wheeler M, Hendon HH (2004) An all-season real-time multivariate MJO index: development of an index for monitoring and prediction. Mon Weather Rev 132:1917–1932
Wheeler M, Kiladis GN (1999) Convectively coupled equatorial waves: analysis of clouds and temperature in the wavenumber–frequency domain. J Atmos Sci 56:374–399
Woolnough SJ, Slingo JM, Hoskins BJ (2001) The organization of tropical convection by intraseasonal sea surface temperature anomalies. Q J R Meteorol Soc 127:888–907
Xavier PK (2012) Intraseasonal convective moistening in CMIP3 Models. J Clim 25:2569–2577
Zhang C (2005) Madden-Julian oscillation. Rev Geophys 43:RG2003
Zhang C, Dong M (2004) Seasonality in the Madden–Julian oscillation. J Clim 17:3169–3180
Zhang C, Hagos SM (2009) Bimodal structure and variability of large-scale diabatic heating in the tropics. J Atmos Sci 66:3621–3640
Zhang GJ, Mu M (2005) Simulation of the Madden–Julian oscillation in the NCAR CCM3 using a revised Zhang–McFarlane convection parameterization scheme. J Clim 18:4046–4064

Zhang C, Dong M, Gualdi S, Hendon HH, Maloney ED, Marshall A, Sperber KR, Wang W (2006) Simulations of the Madden–Julian oscillation in four pairs of coupled and uncoupled global models. Clim Dyn 27:573–592

Zhu H, Hendon H, Jakob C (2009) Convection in a parameterized and superparameterized model and its role in the representation of the MJO. J Atmos Sci 66:2796–2811